

MODELING AND ANALYSIS OF GEOMETRICALLY COMPLEX CORROSION
DAMAGE

A Thesis Presented to
The Faculty of the School of Engineering and Applied Science
University of Virginia

In Partial Fulfillment
of the requirements for the Degree
Masters of Science (Materials Science and Engineering)

by

Colin Tattersall

May 2018

Abstract

In order to validate computational models of corrosion, quantitative assessment of corrosion damage is needed. This thesis describes work addressing these two issues: (a) develop and exercise an open-source algorithm to analyze corrosion damage revealed in cross-sections of corroded specimens, and (b) develop and exercise a computational framework for calculation of potential and current distributions on complex geometrical structures involving galvanic couples under thin electrolyte layer conditions.

A digital image processing method has been developed using MATLAB to perform several tasks that researchers could find useful on cross sectional images. This method takes a RGB image and outputs valuable data on the depth profile. This information can be presented as an area ratio, a depth profile, or a histogram of damage occurred. This method has shown to be accurate, adaptable, and efficient compared to other methods.

A geometrically complex model was constructed in COMSOLTM to investigate the effects of sample geometry, including spacing between fasteners and their location relative to the edges of the sample, as well as water layer thickness. This complex model is based on the NAVAIR galvanic corrosion assembly and utilizes the secondary current distribution framework in COMSOLTM to simulate various scenarios using real-life experimental data for the boundary conditions. Galvanic interaction between the fasteners was observed and the intensity of attack was most severe at the edge of the hole.

Table of Contents

Abstract.....	2
List of Figures.....	5
List of Tables	6
1 Introduction.....	7
1.1 Galvanic Corrosion	7
1.2 Pitting Corrosion.....	8
1.3 Intergranular Corrosion (IGC)	10
1.4 Aluminum Alloys.....	10
1.5 Modeling and Simulation.....	11
1.6 Image Analysis.....	12
1.7 Research Needs and Approaches	12
1.8 Objective Statement	12
1.9 Thesis Organization	12
1.10 References.....	13
2 Automated Quantification of Corrosion Damage from Cross-sectional Micrographs.....	15
2.1 Abstract.....	15
2.2 Introduction.....	15
2.3 Materials and Methods.....	16
<i>Specifications of Computer Used</i>	16
<i>Image Processing</i>	17
2.4 Results.....	20
<i>Depth Profile</i>	20
<i>Total Area Corroded</i>	20
<i>Histogram of Damage</i>	22
<i>Error Comparison</i>	22
<i>Tilted Images</i>	24
2.5 Discussion	25
<i>Accuracy</i>	25
<i>Time of Processing</i>	26
<i>Alternative Comparison</i>	26
<i>Limits</i>	27
2.6 Conclusion	27

2.7	References.....	28
3	Computational studies of potential and current distributions on complex geometrical structures involving galvanic couples under thin electrolyte layer conditions	29
3.1	Abstract.....	29
3.2	Introduction.....	29
3.3	Method and Materials	30
	<i>Galvanic Corrosion Assembly</i>	30
	<i>Three-dimensional finite element analysis (FEA) computational modeling</i>	32
	<i>Construction of model in COMSOL</i>	34
	<i>Materials</i>	35
3.4	Results.....	36
	<i>Water Layer Effects</i>	37
	<i>Conformal vs Uniform Water Layer</i>	38
	<i>Edge Effects</i>	40
	<i>Scribe Effect on Hole</i>	40
	<i>Effect of Sol-gel Application</i>	45
	<i>Effects of Boundary Condition Variability</i>	47
3.5	Discussion	47
	<i>Geometric Effects</i>	48
	<i>Boundary Condition Effects</i>	49
3.6	Conclusion	49
3.7	References.....	50
4	Summary, Technological Impact, & Recommendations for Future Work	51
4.1	Summary	51
	<i>Chapter 2: Automated Quantification of Corrosion Damage from Cross-sectional Micrographs</i>	51
	<i>Chapter 3: Computational studies of potential and current distributions on complex geometrical structures involving galvanic couples under thin electrolyte layer conditions</i>	51
4.2	Technological Impact.....	51
4.3	Recommendations for Future Work.....	53
4.4	References.....	54
5	Appendix.....	55
5.1	Algorithm.....	55
5.2	User Manual.....	56
	Objective.....	56

How to Use	56
Rotated Pictures	60
More on Exporting	61

List of Figures

Figure 1.1 ⁴ : Polarization curves of iron and zinc being analyzed for galvanic coupling behavior.	8
Figure 1.2 ⁸ : Illustration of pit corrosion on an aluminum surface.	9
Figure 1.3 ¹¹ : Different pit sizes and shapes found through cross-sections.	9
Figure 1.4: Schematic for the layout of this thesis.....	13
Figure 2.1: (a) Original RGB image. (b) Greyscale image. (c) Binary Image. (d) Image after a fill-in operation has been performed. (e) Image with border of damage in white. (f) Example depth profile output from border in (e).	19
Figure 2.2: Depth profile of a cross section from a corroded AA7075-T6 alloy.....	20
Figure 2.3: (a) Demonstrates the manual measurement of the height and width measurements done by the algorithm. (b) Shows the total area calculated within the highlighted boundary in pixels.	21
Figure 2.4: Output for the histogram of damage for the sample found in Figure 3.....	22
Figure 2.5: (a) Comparison of the depth measured by the algorithm and by a manual method utilizing ImageJ on the image from Figure 1. (b) Demonstration of manual measurements. (c) Image containing heavy fissure morphology with algorithm's border detection overlaid in red. (d) Image containing undercutting with algorithm's border detection overlaid in red. (e) Image with a slight angle along the surface with the algorithm's border detection overlaid in blue.	24
Figure 2.6: (a) Depth profile obtained from image in 5e demonstrating the angled tilt. (b) Histogram of damage from 6a showing the effect that a slight tilt has on the damage distribution. (c) Depth profile obtained after fixing for angled tilt. (d) Histogram of damage from 6c.	25
Figure 3.1: (a) NAVAIR galvanic corrosion assembly schematic ⁶ . (b) Schematic of the bolt to panel with the measurements found in Table 1&2. (c) Schematic of the spacing between fastener, washer, and panel with measurement used highlighted in red.....	32
Figure 3.2: COMSOL model geometry of the NAVAIR galvanic corrosion assembly.	34
Figure 3.3: Final construction of the NAVAIR galvanic corrosion assembly.....	35
Figure 3.4: Polarization curves provided by Luna Innovations at 35C and 5% NaCl before activation of the AA7075-T651 and after activation of the AA7075-T651.	36
Figure 3.5: (a) Geometric layout of the three locations to be measured at varying water layer thicknesses. (b)Current Density distribution as a function of water layer thickness at three distinct locations found in (a).	38

Figure 3.6: (a) Uniform water layer. (b) Conformal water layer. (Current densities are measured in A/m^2).....	39
Figure 3.7: Current density false color plot of the full NAVAIR galvanic corrosion assembly showing the effect the edge has on the distribution.....	40
Figure 3.8: Illustration of the areas where the AA075-T6 boundary conditions were implemented in blue.....	41
Figure 3.9: (a) Illustration of the two scribe locations where the data is being obtained inside of the blue and green circle. (b) Current density distribution correlating to the colored circles in (a).	42
Figure 3.10: Illustration of the areas where the AA075-T6 boundary conditions were implemented in blue.....	43
Figure 3.11: (a) Illustration of the path the data was obtained for (b) The current density distribution following the path illustrated in (a).	44
Figure 3.12: Current Density distribution comparing the two scenarios from Figures 8 & 10. ...	45
Figure 3.13: (a) Images with colored lines correlating to the data in (b) and (c). (b) Current density distribution of the bare case with the color of the line corresponding to the lines in (a). (c) Current density distribution of the sol-gel case.	46
Figure 3.14: (a) Current density distribution with both boundary condition scenarios. (b) Current density distribution using the AA7075 boundary condition after activation.....	47

List of Tables

Table 3.1: Measurements of the outer and inner diameters of the washers.....	32
Table 3.2: Measurements of the different fastener parts.....	32

1 Introduction

1.1 Galvanic Corrosion

Galvanic corrosion is an electrochemical process that takes place when two metals of different standard electrode potential values are in electrical or physical contact in the presence of an electrolytic solution¹. This potential difference between the two metals promotes a reduction-oxidation reaction where the more noble (more positive) metal behaves as the cathode and the more active (more negative) metal behaves like the anode. This coupled anode will experience an accelerated corrosion rate compared to if it was left uncoupled.

Mixed potential theory is the most commonly used way to predict galvanic corrosion behavior. This theory consists of two assumptions, the first being that any electrochemical reaction can be broken down into partial reduction and oxidation reactions and the second being the electric charge is conserved (i.e., there is no accumulation of electrical charge within the system)^{2,3}. Due to this latter point, the cathodic and anodic corrosion rates must be equal and from this by increasing the size of the cathode, the anodic rate of dissolution increases. This can be seen in Figure 1.1, which shows the coupling of iron, acting as cathode, and zinc, acting as anode, where the I_{CORR} increases and the E_{CORR} becomes more positive as the size of the cathode is increased. The increase in current density causes the acceleration of intergranular corrosion (IGC) on the anode⁴. The limitations of mixed potential theory causes its applications to be used on galvanic systems with simple geometry as more complex geometries require more complicated techniques, such as finite element analysis (FEA) modeling to account for the ohmic drop in potential and current distributions.

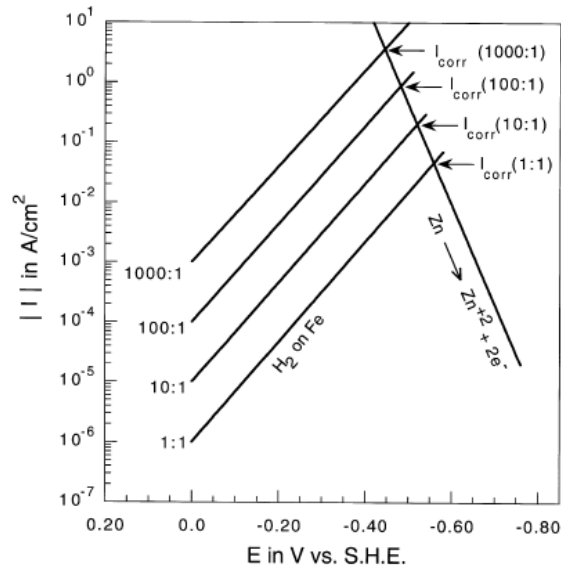


Figure 1.1⁴: Polarization curves of iron and zinc being analyzed for galvanic coupling behavior.

1.2 Pitting Corrosion

Pitting corrosion is a type of localized corrosion that leads to the development of small holes in a metal⁵. These pits are commonly found underneath the surface deposits caused by the accumulation of corrosion products. When a metal is in an environment containing oxygen, an active metal will form an oxide layer that will help prevent further corrosion. When this oxide film is damaged (i.e., scratch), a new oxide layer will form on that surface of the metal due to the re-passivation rate being higher than the corrosion rate^{6, 7}. The pitting is propagated from a weak point in the oxide layer by the attack of a halide ion^{9, 10}. Figure 1.2 illustrates an example of pitting corrosion with the oxidation of the aluminum anode leading to the formation of the aluminum ion, Al^{3+} , which combines with the chloride ions to form aluminum chloride and the free electron moves to the cathode to reduce the hydrogen cation leading to the formation of hydrogen gas. Also, the oxygen reduction takes place at the intermetallic particle forming the hydroxyl ion. The formation of $\text{Al}(\text{OH})_3$ prevents oxygen from reacting with the metal and the chloride ions will

migrate into the pit. When the AlCl_3 is hydrolyzed, the electrolytic solution becomes more acidic, accelerating pit propagation. The concurrent reduction reaction causes local alkalization around the intermetallic particle, leading to the dissolution of the aluminum. Due to how pits are formed, the size and shape of a pit varies greatly leading to the need to identify them through metallography where the pit is cross-sectioned. Fig 1.3 shows different sizes and shapes of pits that can be found through cross-sections.

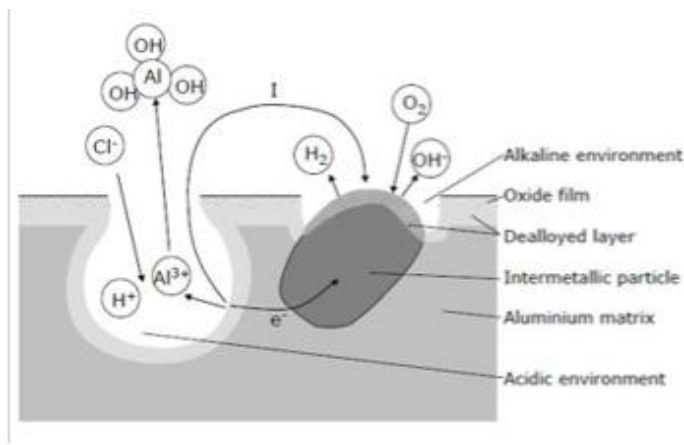


Figure 1.2⁸: Illustration of pit corrosion on an aluminum surface.

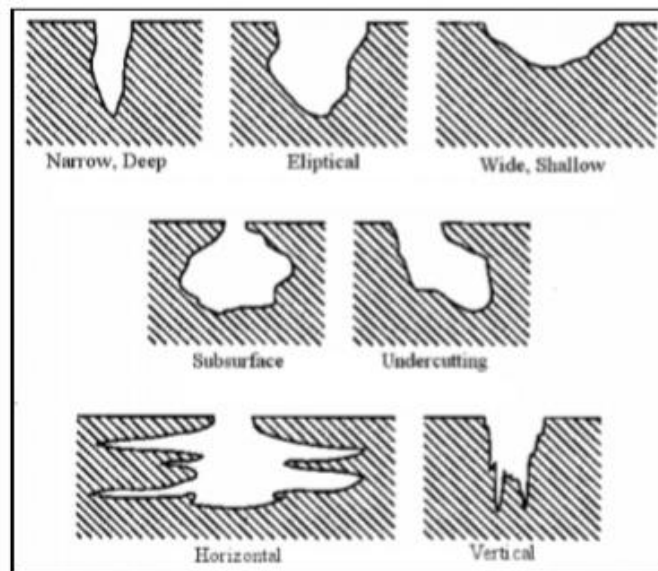


Figure 1.3¹¹: Different pit sizes and shapes found through cross-sections.

1.3 Intergranular Corrosion (IGC)

Intergranular corrosion occurs when there is a selective dissolution of the grain boundary zone when the bulk grain of the metal is not attacked¹². IGC susceptibility depends on the metal composition and how it was thermodynamically processed. In general, grain boundaries are the sites for precipitation and segregation, which will make the boundaries chemically and physically different than the matrix that surrounds them. Due to this, the accumulation of these impurities are what cause the corrosion.

1.4 Aluminum Alloys

Aluminum alloys are widely used in the aircraft and naval industry due to their low density, high strength, and relatively low cost. This attractiveness stems from their ability to be easily made. These aluminum alloys are classified as being either heat treatable or non-heat treatable¹². Heat-treatable alloys are ones that can be strengthened through a controlled cycle of heating and cooling, however this increase of strength comes with a decrease in formability. Non heat treatable alloys are hardened by cold working with some additional strength coming from the alloying elements and work hardening. Additional classification of the aluminum alloys comes from the chemical composition resulting in a four-digit numerical designation system depending on the major alloying element^{12,13}. This classification is as follows: 2XXX-copper, 3XXX-manganese, 4XXX-silicon, 5XXX-magnesium, 6XXX-magnesium and silicon, 7XXX-zinc. Out of these classifications, 2XXX, 5XXX, and 7XXX are the most popular. Each of these alloying elements are used for different reasons depending on the property that is wanted¹²⁻²⁰. For example, the 7XXX series, an Al-Zn-Mg-Cu alloy, the zinc and magnesium are used to control the ageing process, meanwhile the copper is to increase the ageing rate. The copper inclusion will also reduce the effective resistance against general corrosion, however will

increase the resistance to stress corrosion¹². Due to the alloying and work hardening, second phases are typically present at the grain boundaries and can either be anodic to the matrix in the cases for the 2XXX and 5XXX series, or cathodic to the matrix in the cases for the 2XXX and 7XXX series. In both of these cases, there will be a micro-galvanic couple at the grain boundaries increasing the susceptibility to intergranular corrosion.

1.5 Modeling and Simulation

Modeling and simulation has been around for quite a while, however in 2006 the NSF report on “Simulation-Based Engineering Science” demonstrated the potential of utilizing modeling and simulations to change the way engineering science is approached¹⁵. The reason for the increasing interest into simulations is stemmed from the following reasons: (1) the use of simulations is cheaper, safer, and on rare occasions more ethical than conducting real-world experiments. (2) Due to the ability to control the configuration of environmental parameters, simulations can be more realistic than traditional experiments. (3) The speed of a simulation, depending on the complexity, is sometimes faster than a traditional experiment.

In this work, a finite element analysis (FEA) modeling software COMSOLTM (COMSOL Inc. Stockholm, Sweden) is used. FEA determines the solution to a set of coupled partial differential equations by dividing the physical domain of interest into a collection of subdomains. The behavior of these subdomains is represented by a set of governing equations and are systematically recombined into a global system of equations that will be used for a final calculation. This global system of equations has known solution techniques and can be calculated through the use of an initial value, or a guess, that a user inputs.

1.6 Image Analysis

Image analysis includes the processing of an image into several fundamental components in order to extract statistical data¹⁶. It can be used to accomplish such tasks as: finding shapes, removing noise, detecting edges, counting objects, and measuring regions. This term “image analysis” is a broad term that encompasses different techniques that accomplish tasks listed previously. These techniques are: image enhancement which is used help remove noise, image segmentation which is used to isolate regions and objects of interest, and region analysis which is used to help extract statistical data.

1.7 Research Needs and Approaches

As summarized, there is a need in corrosion studies for the quantification of corrosion damage morphology found with IGC and pit corrosion and a need to be able to predict galvanic corrosion damage by utilizing mixed potential theory on complex geometries. In order to do both of these, an open-sourced image analysis algorithm was developed on MATLABTM for the former and for the latter a FEA model was built using COMSOLTM framework.

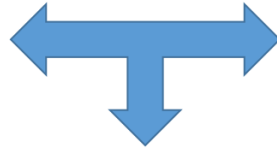
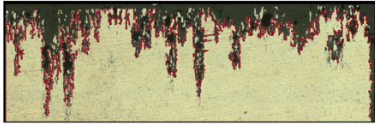
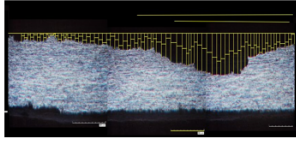
1.8 Objective Statement

The main goal of this thesis is to address the needs of a tool for quantification of damage morphologies found within cross-sectional images and a geometrically complex model of galvanic corrosion.

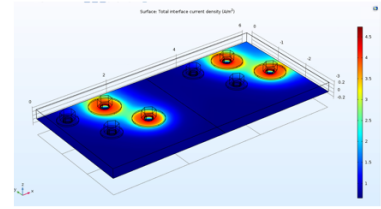
1.9 Thesis Organization

Figure 1.4 depicts a schematic for the layout of this thesis, “The Modeling and Analysis of Complex Corrosion Damage”.

Chapter 2: Automated Quantification of Corrosion Damage from Cross-Sectional Micrographs



Chapter 3: Computational studies of potential and current distributions on complex geometrical structures involving galvanic couples under thin electrolyte layer conditions



Chapter 4: Summary, Technological Impact, & Recommendations for Future Work

Figure 1.4: Schematic for the layout of this thesis.

Chapter 2 presents a damage quantification algorithm developed in MATLAB™. The ability and flexibility of this algorithm are demonstrated.

Chapter 3 presents a complex FEA model of a galvanic corrosion assembly constructed in COMSOL™. The effects of sample geometry, including spacing between fasteners and their location relative to the edges of the sample, as well as water layer thickness are investigated.

Chapter 4 summarizes the conclusions and ties in results from each chapter. The technological impacts and recommendations for future work are also explored.

1.10 References

1. Chang, R.. 1991. Chemistry, 4* Edition. McGraw-Hill Inc.. New York
2. J. R. Davis, in Corros. Alum. Alum. Alloy., ASM International, 1999, p. 110
3. N. Perez, in Electrochem. Corros. Sci., Springe, 2004, p. 155.
4. McCafferty, E. *Introduction to Corrosion Science*. (2009).
5. G. S. Frankel, J. Electrochem. Soc. 145 (1998) 2186.
6. K. Shimizu, R.C. Furneaux, G.E. Thompson, G.C. Wood, A. Gotahr, K. Kobayashi, *oxid. of Met.* 35 (1991) 427.
7. J.R. Davis, et. al, editor, *Metals Handbook*, ninth edition, ASM International, Ohio, 13 (1987) pages 104-122 and 583-609.
8. *Lessons Learned from Civil Aviation Accidents*.
http://lessonslearned.faa.gov/ll_main.cfm?TabID=2&LLID=75&LLTypeID=2

9. K. Nisancioglu, corrosion of aluminium alloys, Proceedings of ICAA3, Trondheim, NTH and SINTEF 3 (1992) 23
10. G. M. Scamans, J.A. Hunter, N.J.H. Holroyd, Corrosion of Aluminum - a New Approach, Proceedings of 8th International Light Metals Congress, Leoben-Wien, (1987) 699.
11. G. Bergmann, L.T. Waugh, L. Pauling, Acta Cryst. 10 (1957) 254.
12. J.E. Hatch, editor. Aluminium Properties and physical metallurgy, ASM, Ohio, (1984) 242.
13. Davis JR (1994) Aluminum and aluminum alloys. ASM Speciality Handbook, ASM International, Materials Park, OH, USA
14. Vasudevan AK, Doherty RD (1989) Aluminum alloys—contemporary research and applications. Academic Press, Inc, Cambridge, MA, USA
15. F. Sato and R. C. Newman, Corrosion (Houston), 55, 3 (1999).
16. M. Zamin, Corrosion (Houston), 37, 627 (1981).
17. B. Mazurkiewicz and A. Piotrowski, Corros. Sci., 23, 697 (1983).
18. O. Seri, Corros. Sci., 36, 1789 (1994).
19. J. R. Scully, T. O. Knight, R. G. Buchheit, and D. E. Peebles, Corros. Sci., 35, 185 (1993).
20. K. Nişancıoğlu, J. Electrochem. Soc., 137, 69 (1990).
21. "Report on Simulation-Based Engineering Science" (PDF). National Science Foundation (NSF) Blue Ribbon Panel. 2006-05-01.
22. Image Analysis. <https://www.mathworks.com/discovery/image-analysis.html>

2 Automated Quantification of Corrosion Damage from Cross-sectional Micrographs

2.1 Abstract

A digital image processing method has been developed using MATLAB to perform several tasks that researchers could find useful on cross sectional images. This method takes a RGB image and outputs valuable data on the depth profile. This information can be presented as an area ratio, a depth profile, or a histogram of damage occurred. This method has shown to be accurate, adaptable, and efficient compared to other methods. This algorithm can be found at <https://github.com/ctatt19/CorrosionTool>.

2.2 Introduction

Corrosion damage morphology can range on a continuum from highly localized (e.g., pitting, intergranular corrosion) to uniform dissolution. Quantitative assessment of corrosion damage has typically involved either mass loss (for uniform corrosion)¹⁻³ or optical profilometry (for localized corrosion)^{4,5}. Corrosion does more than just cause a metal to lose mass, it damages morphology and surface distribution which are both influenced by many different factors and depending on the severity of the damage, a fracture can occur. Therefore, in order to understand the scope of the morphological damage that occurs on a certain metal, visual examination is needed. Currently there is a method to classify morphological changes caused by pitting by use of the ASTM G-46. Previous work has been done utilizing this classification in order to classify shape and size of pits from a cross sectional image¹³. However, to fully assess corrosion damage morphology there is a need to extract quantitative data from an image.

Image processing allows for the extraction of data from a digital image and the ability to calculate different parameters associated with morphology. Approaches to evaluating images can be categorized as manual and semi-automatic. Manual approaches that rely on the program

ImageJ⁶, or other similar products, that allow the user to measure lengths and areas with plug-ins, are time and labor intensive and are thus not suitable for the high throughput analysis that is required when looking at the morphological changes that occur with corrosion. Semi-automatic approaches for classifying morphology tend to be included within an expensive software package that allows for some flexibility in obtaining the data you want such as Nikon's Element-NIS or do not apply to corrosion morphology, such as RootAnalyzer⁷, which characterizes root cells and tissues, and are close-sourced. Due to the need for an inexpensive tool to help assist with obtaining data on morphological damage to a surface, an algorithm was developed in Matlab specifically for corrosion damage morphology and to be open-sourced as to allow other researchers the ability to make changes to suit their needs.

The algorithm presented in this paper has been developed to quickly and accurately perform several tasks that researchers could find useful. These tasks include: depth profile, total area corroded, max depth, average depth, and a histogram of damage depth.

2.3 Materials and Methods

Specifications of Computer Used

All of the computations were performed on a machine with an Intel®Core™i7-6700K CPU.

Samples Analyzed

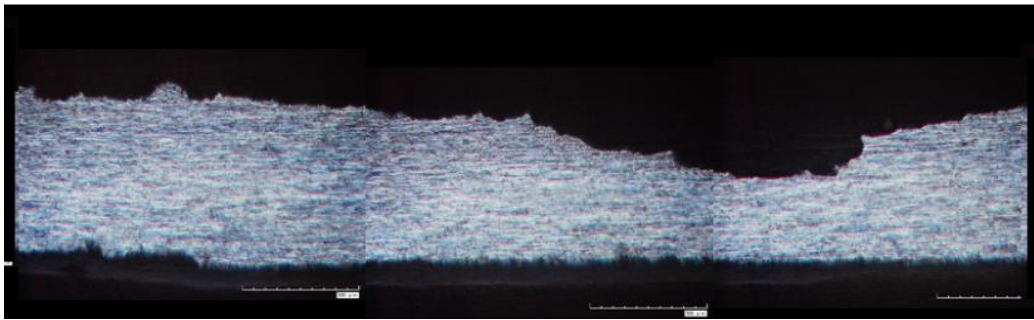
The cross-sectional images that were used with this algorithm include AA7075-T6⁸, AA5556-H116⁹, and sensitized AA5083¹⁰.

Image Processing

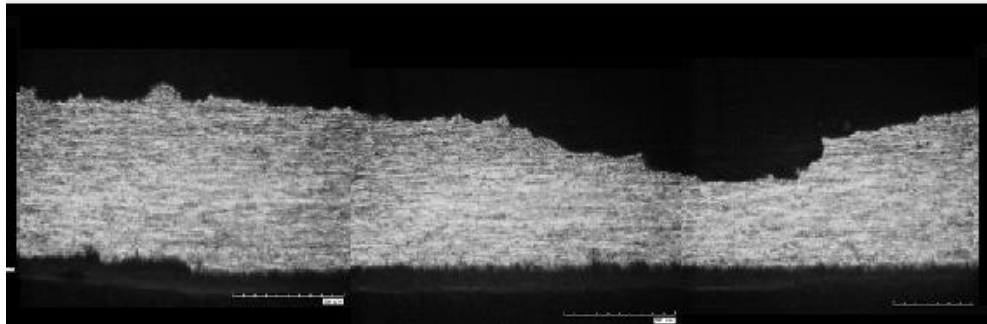
The procedure to obtain the data to be used involves several image processing steps to produce results without the need to do any manual inputs and has the capability to handle either an individual or montage of images. The first step of the algorithm is to convert an RGB image (Figure 2.1a) to a grayscale map by removing hue and saturation information and keeping the luminance information from an image (Figure 2.1b). The algorithm used to calculate the grayscale values is identical to that in the Recommendation of the International Telecommunication Union Radio communication Sector BT.601-7¹¹. This step is crucial as it converts the 3D pixel value of a RGB image to a 1D value, which allows for better edge detection and reduces the complexity required moving forward. The next step is to take this grayscale image and convert it into a binary image (Figure 2.1c). The output is an image where every pixel with a luminance value greater than the signal value to be white and every value lower to be black. This value is determined by Otsu's method¹² utilizing a 256-bin image histogram. This step allows the procedure to remove the background by making it completely white and the object in question to be easily identified. The next step is to remove small connected objects that have less connectivity, meaning the white pixel groupings that do not reach a certain threshold are filled in as a means to remove artifacts that could be due to the original image quality or preparation of the sample (Figure 2.1d). Following this, the pixels where white meet black pixels are enlarged and the rest are removed allowing for the detection of a border (Figure 2.1e). Once the border is detected, the procedure is able to utilize this data in order to obtain usable information, such as depth profiles (Figure 2.1f). To do this, the program finds the two edges of sample and determines the baseline from which to determine the change in morphology of the sample's surface automatically. If the sample's surface does not have an unchanged section, manual input is able to be implemented. This process will

output a data set with the difference between the baseline and the boundary's pixels. To determine the actual change in microns, or any other scale, the program measures the scale bar in pixels.

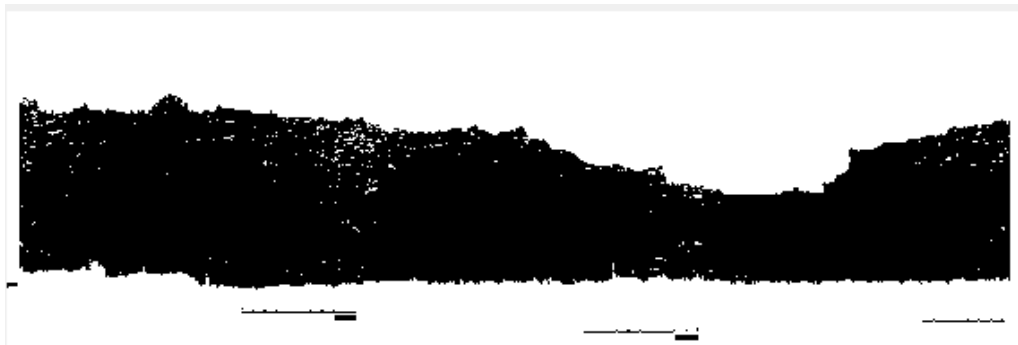
All of these steps are performed on Matlab and the data are stored within the workspace on the application, however there is an option to output the data as either an Excel worksheet or a CSV file.



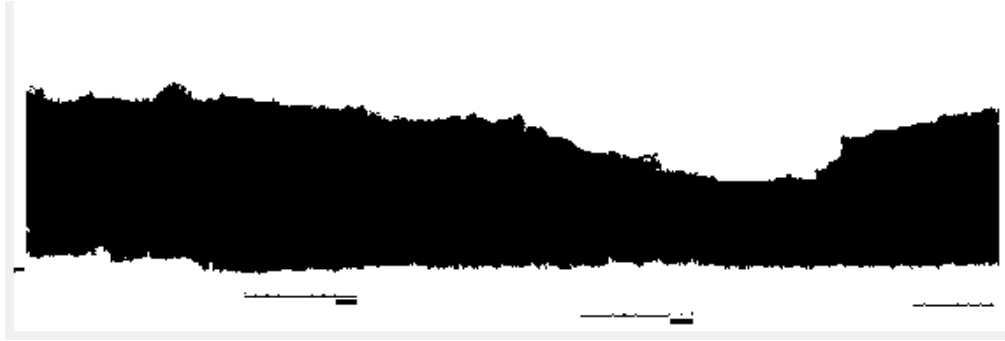
(a)



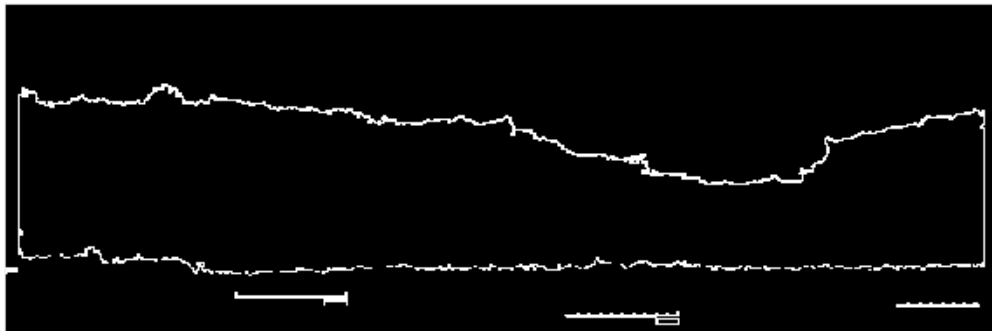
(b)



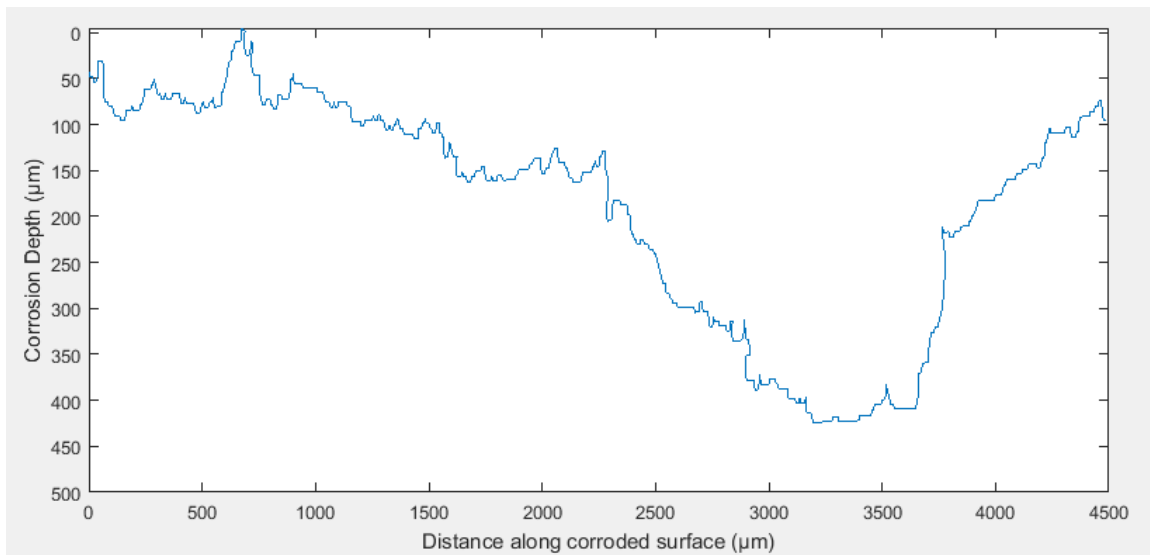
(c)



(d)



(e)



(f)

Figure 2.1: (a) Original RGB image. (b) Greyscale image. (c) Binary Image. (d) Image after a fill-in operation has been performed. (e) Image with border of damage in white. (f) Example depth profile output from border in (e).

2.4 Results

This algorithm was applied to many different types of corrosion morphology cross section images. After application of the algorithm, the results were compared to manually obtained values as a way of verifying the accuracy of the algorithm. The results shown are examples of each of the tasks aforementioned.

Depth Profile

Figure 2.2 shows the depth profile of a cross section of an AA7075 sample⁸. Along with this depth profile, values of max depth and average depth were also calculated to be 893.51 microns and 381.04 microns respectively.

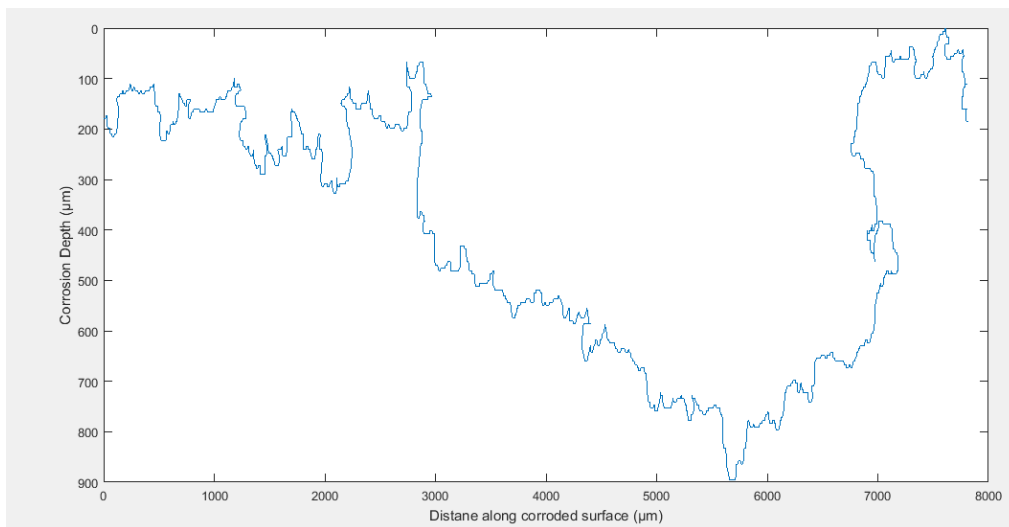
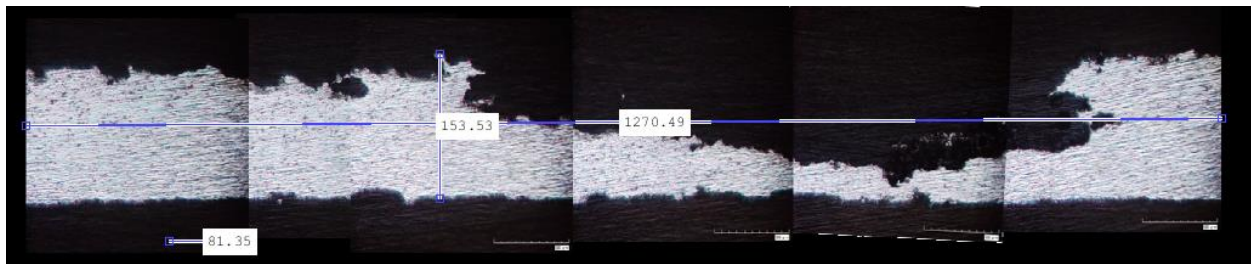


Figure 2.2: Depth profile of a cross section from a corroded AA7075-T6 alloy.

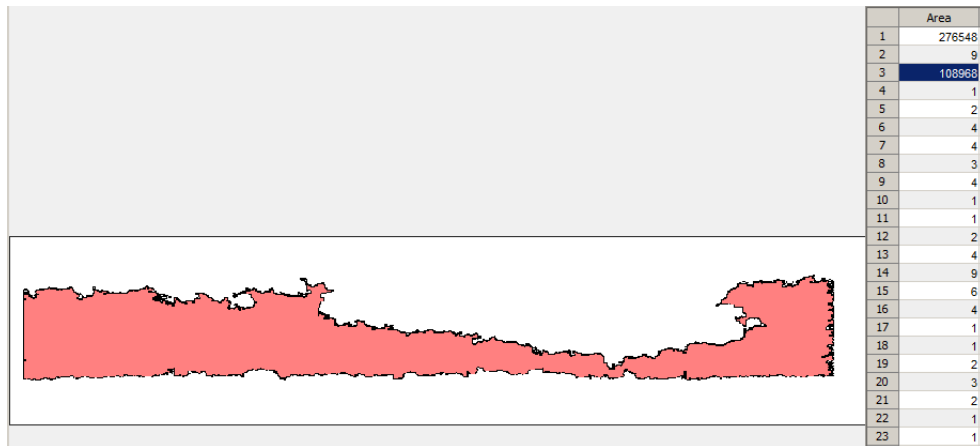
Total Area Corroded

Figure 2.3 demonstrates how the total area corroded was measured. Measurement of the total area corroded is done by obtaining starting total area by calculating the size of the sample by its height and width, which is obtained by the algorithm determining the highest point of the sample

and its width, found by determining the distance between the two edges of the sample. It then subtracts this value by the total area of the boundary. To illustrate this, Figure 2.3a shows the manual measurement of the height and width measurements done by the program and Figure 2.3b shows the total area calculated within the boundary. Each of these measurements are in pixels and will have to be converted to microns, or the choice of measurement, through the scale bar measurement also demonstrated in Figure 2.2a. Figure 2.3's total area corroded is $3,224,410\mu\text{m}^2$ or 44% of the total area.



(a)



(b)

Figure 2.3: (a) Demonstrates the manual measurement of the height and width measurements done by the algorithm. (b) Shows the total area calculated within the highlighted boundary in pixels.

Histogram of Damage

Figure 2.4 shows the output for the histogram of damage for the sample shown in Figure 2.3. This histogram was calculated by using the depth profile in Figure 2.2. This histogram shows the frequency in which a pixel was measured on the border of having a value between 0 and the max depth.

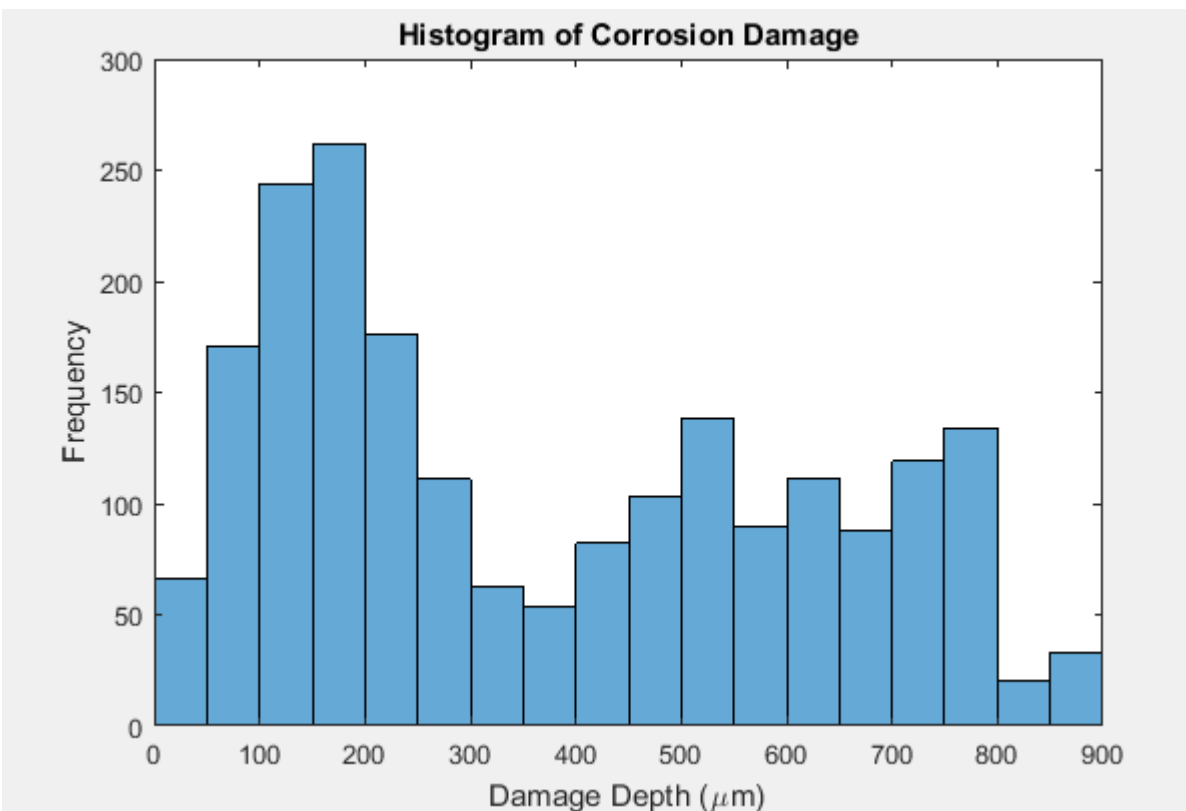
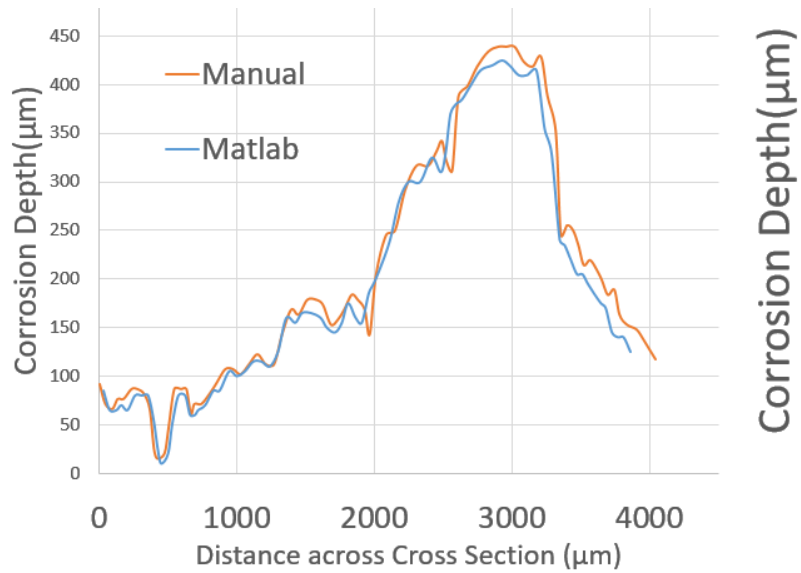


Figure 2.4: Output for the histogram of damage for the sample found in Figure 3

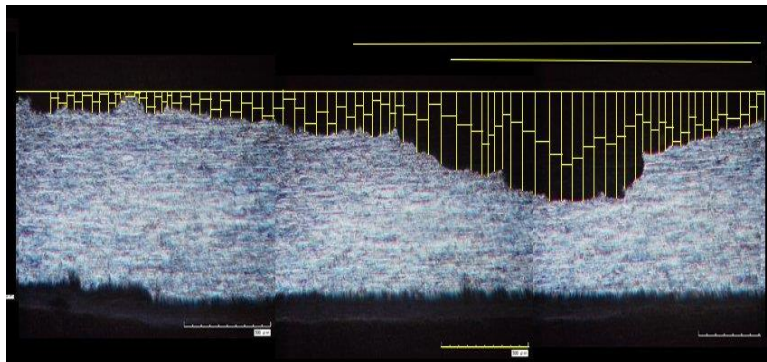
Error Comparison

To demonstrate how accurate the program is Figure 2.5a has a comparison of the depth measured by the algorithm and by a manual method utilizing ImageJ on the image from Figure 2.1. Figure 2.5b shows the manual method measurements, with the vertical lines determining the depth from the baseline and the small horizontal lines between them determining the space

between each. Figure 2.5c-e show how the border matches up against several different types of images. Figure 2.5c is an image showing heavy fissure morphology¹⁰, 2.5d is against an image with undercutting⁸ and 2.5e is against an image that has a slight angle to it⁹.



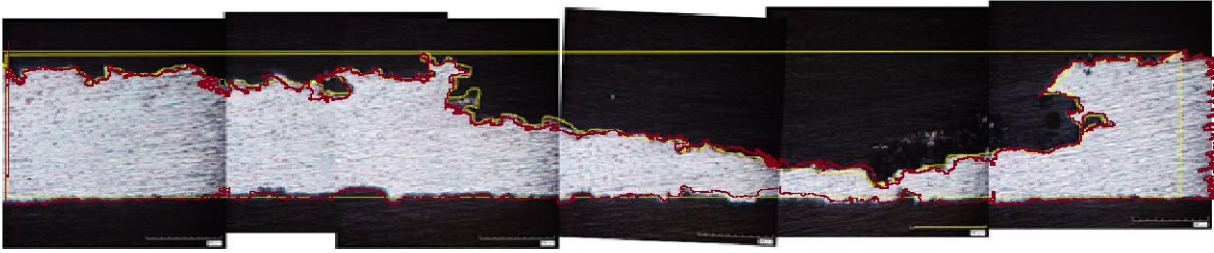
(a)



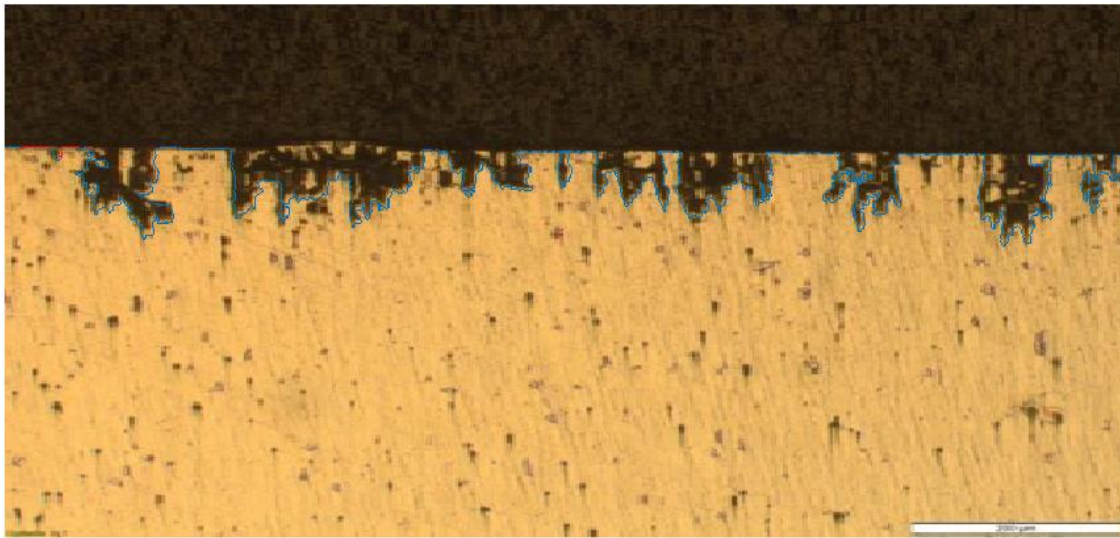
(b)



(c)



(d)



(e)

Figure 2.5: (a) Comparison of the depth measured by the algorithm and by a manual method utilizing ImageJ on the image from Figure 1. (b) Demonstration of manual measurements. (c) Image containing heavy fissure morphology with algorithm's border detection overlaid in red. (d) Image containing undercutting with algorithm's border detection overlaid in red. (e) Image with a slight angle along the surface with the algorithm's border detection overlaid in blue.

Tilted Images

Figure 2.6 demonstrates the ability of the algorithm to correct for tilt and how it changes a data set, such as the histogram of damage. Figure 2.6a shows the depth profile of Figure 2.5e with no tilt correction with the baseline drawn in black. Figure 2.6b shows the histogram of this image.

Figure 2.6c shows the depth profile with tilt correction with the baseline in black. Figure 2.6d shows the histogram of this image.

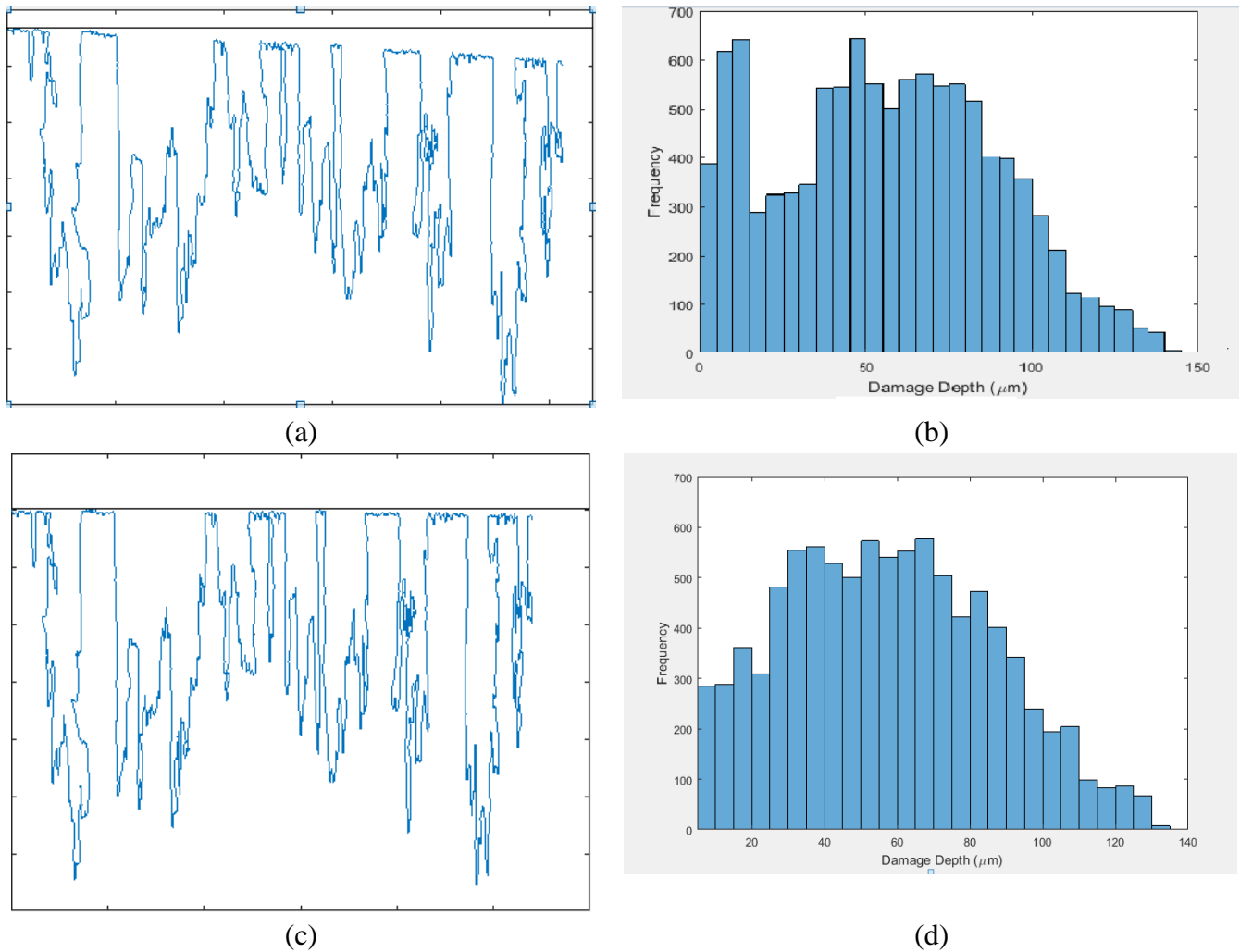


Figure 2.6: (a) Depth profile obtained from image in 5e demonstrating the angled tilt. (b) Histogram of damage from 6a showing the effect that a slight tilt has on the damage distribution. (c) Depth profile obtained after fixing for angled tilt. (d) Histogram of damage from 6c.

2.5 Discussion

Accuracy

Quantitative results obtained from the program are compared to the manually obtained results and are found to be greater than 95% accurate for most cases barring compromised image quality or inaccurate manual measurements.

Time of Processing

The processing time for these photos varied, depending on the size and quality of each image ranging from 10 seconds to 60 seconds. In comparison, manual measurements took between 1 hour and 3 hours depending on the complexity and size of the image. As mentioned, with the accuracy being greater than 95% in a majority of the images analyzed, reducing the amount of time spent to obtain comparable data will allow for the ability to analyze a large amount of images allowing for better classification of corrosion damage morphology.

Alternative Comparison

There are currently only a few options that are similar to the method proposed here, however each has their own pitfalls and benefits. There is a processing method proposed in [link to paper describing method](#) for the image processing method for morphology characterization and pitting corrosion evaluation. However this method is quite limited to just characterizing the type of pit size and shape. For methods that have the capability to possibly perform similar tasks the algorithm in this paper can do, ImageJ and Nikon's NIS-Elements would two of the better choices.

ImageJ is a free open source program written in Java that has a large online community. ImageJ allows the use of different plug-ins that help a user obtain the data they desire. This program most likely has the capability to develop an algorithm much like the one presented here, if the user has enough knowledge in Java. Nikon's NIS-Elements is a commercial application that features many of the tasks the algorithm presented here can do in a commercial package. However, that program is close-sourced and does not allow the ability to add onto the algorithm, unlike Matlab and ImageJ where you can add anything to the algorithm, if you know how to. Using these two alternatives to obtain the same amount of data that the algorithm in this paper does would require a lot of work and knowledge of each of their individual languages. What this program

does is quickly and automatically obtains the depth profile, the total area corroded, corrects for tilt, and produces a histogram of the depth profile. This is done within a program, Matlab, which is heavily used in higher education allowing for easy first-time use. Similar to ImageJ, Matlab has a huge online community of willing helpers and a large website detailing what each command in its library does. This allows for a user to troubleshoot their own problem and change the algorithm to fit their needs.

Limits

This algorithm with all of its benefits does suffer from limitations that require the user to use their best judgement when assessing the data collected. These limitations include the accuracy of the algorithm when used with blurry images, fissures that are narrower than the resolution of the algorithm which is about 2 pixels, and differentiating between tilt and surface roughness. Though with these limitations on the algorithm, these problems can be fixed in most cases through taking more images at a higher magnification in order to give a higher resolution.

2.6 Conclusion

This algorithm has shown that it is possible to import a wide variety of images and output valuable information. The tasks that this algorithm is able to perform was shown to perform exceptionally well across a variety of different types of corrosion damage. The algorithm uploaded on GitHub, <https://github.com/ctatt19/CorrosionTool>, to allow for researchers to use the algorithm and make changes on a per case basis. In general, this algorithm is able to be used on a wide variety of images that are commonly found within corrosion studies and allows the researcher to obtain quantifiable data in a quick and accurate way.

2.7 References

1. O. Poupard, V. L'Hostis, S. Catinaud, I. Petre-Lazar, Corrosion damage diagnosis of a reinforced concrete beam after 40 years natural exposure in marine environment, *Cement and Concrete Research*, Volume 36, Issue 3, 2006, Pages 504-520, ISSN 0008-8846, <https://doi.org/10.1016/j.cemconres.2005.11.004>.
2. A.D. King, N. Birbilis, J.R. Scully, Accurate Electrochemical Measurement of Magnesium Corrosion Rates; a Combined Impedance, Mass-Loss and Hydrogen Collection Study, *Electrochimica Acta*, Volume 121, 2014, Pages 394-406, ISSN 0013-4686, <https://doi.org/10.1016/j.electacta.2013.12.124>.
3. A. Pardo, M.C. Merino, A.E. Coy, R. Arrayal, F. Viejo, E. Matykina, Corrosion behaviour of magnesium/aluminium alloys in 3.5wt.% NaCl, *Corrosion Science*, Volume 50, Issue 3, 2008, Pages 823-834, ISSN 0010-938X, <https://doi.org/10.1016/j.corsci.2007.11.005>.
4. Hasan Güleriyüz, Hüseyin Çimenoğlu, Effect of thermal oxidation on corrosion and corrosion-wear behaviour of a Ti-6Al-4V alloy, *Biomaterials*, Volume 25, Issue 16, 2004, Pages 3325-3333, ISSN 0142-9612, <https://doi.org/10.1016/j.biomaterials.2003.10.009>.
5. Amit Biswas, Jyotsna Dutta Majumdar, Surface characterization and mechanical property evaluation of thermally oxidized Ti-6Al-4V, *Materials Characterization*, Volume 60, Issue 6, 2009, Pages 513-518, ISSN 1044-5803, <https://doi.org/10.1016/j.matchar.2008.12.014>.
6. Schneider, C. A.; Rasband, W. S. & Eliceiri, K. W. (2012), "NIH Image to ImageJ: 25 years of image analysis", *Nature methods* **9(7)**: 671-675, PMID 22930834
7. PLoS One. 2015 Sep 23;10(9):e0137655. doi: 10.1371/journal.pone.0137655. eCollection 2015.
8. G. Liu, personal communication.
9. Lindsey Blohm, "Galvanic Coupling of AA5XXX-H116 and CDA 706 Utilizing Laboratory, Outdoor, and Accelerated Testing," MS Thesis, University of Virginia (2018)
10. Mary Lyn Lim, "Intergranular Corrosion Propagation in Sensitized Al-Mg Alloys", PhD Dissertation, University of Virginia (2016).
11. ITU-R BT.601-7 Studio encoding parameters of digital television for standard 4:3 and wide screen 16:9 aspect ratios, 03/11
12. Otsu, N., "A Threshold Selection Method from Gray-Level Histograms," *IEEE Transactions on Systems, Man, and Cybernetics*, Vol. 9, No. 1, 1979, pp. 62-66.
13. E.N. Codaro, R.Z. Nakazato, et al. "An image processing method for morphology characterization and pitting corrosion evaluation" *Material Science and Engineering: A*, Vol. 334, No. 1-2, Sep. 2002, Pages 298-306.

3 Computational studies of potential and current distributions on complex geometrical structures involving galvanic couples under thin electrolyte layer conditions

3.1 Abstract

A geometrically complex model was constructed in COMSOL™ to investigate the effects of sample geometry, including spacing between fasteners and their location relative to the edges of the sample, as well as water layer thickness. This complex model is based on the NAVAIR galvanic corrosion assembly and utilizes the secondary current distribution framework in COMSOL™ to simulate various scenarios using real-life experimental data for the boundary conditions. Galvanic interaction between the fasteners was observed and the intensity of attack was most severe at the edge of the hole.

3.2 Introduction

In modern aircraft, there is a need to protect aluminum structures from galvanic corrosion due to dissimilar metals used in complex aerospace structures. Galvanic corrosion between corrosion resistant fasteners (e.g., stainless steel or titanium alloys) and aluminum alloy structures represent a recurring problem¹⁻⁵. One means of mitigating such attack is via the application of surface treatments to the fasteners designed to limit their cathodic current density. In order to efficiently assess the protective ability surface treatments, finite element analysis modeling (FEA) has been used to predict the current and potential distributions caused by the noble fastener with and without surface treatments. In this way, the important characteristics of the surface treatment can be assessed as well as its likely effectiveness as a function of geometry and environmental variables.

FEA determines the solution to a set of coupled partial differential equations by dividing the physical domain of interest into a collection of subdomains. The behavior of these

subdomains is represented by a set of governing equations and are systematically recombined into a global system of equations that will be used for a final calculation. This global system of equations has known solution techniques and can be calculated through the use of an initial value, or a guess, that a user inputs. COMSOL™ (COMSOL Inc. Stockholm, Sweden) is a commercially available FEA modeling software that includes an electrochemical corrosion module that includes the ability of solving a primary, secondary or tertiary current distribution framework at either a stationary (non-time dependent) or time-dependent scenarios. Primary current distribution accounts only for the voltage losses due to solution resistance and neglects the electrode kinetics and concentration dependent effects. Secondary current distribution accounts for the effect of the electrode kinetics in addition to the solution resistance. Tertiary current distribution accounts for the effect of variations in electrolyte composition and ionic strength on the electrochemical process, in addition to the solution resistance and electrode kinetics found in the secondary current distribution.

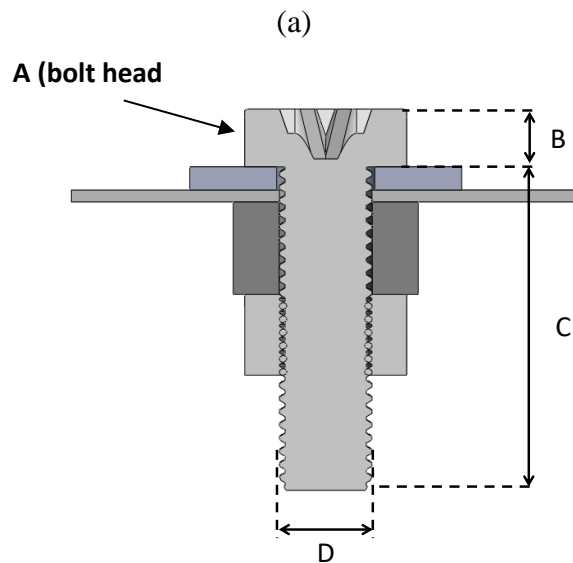
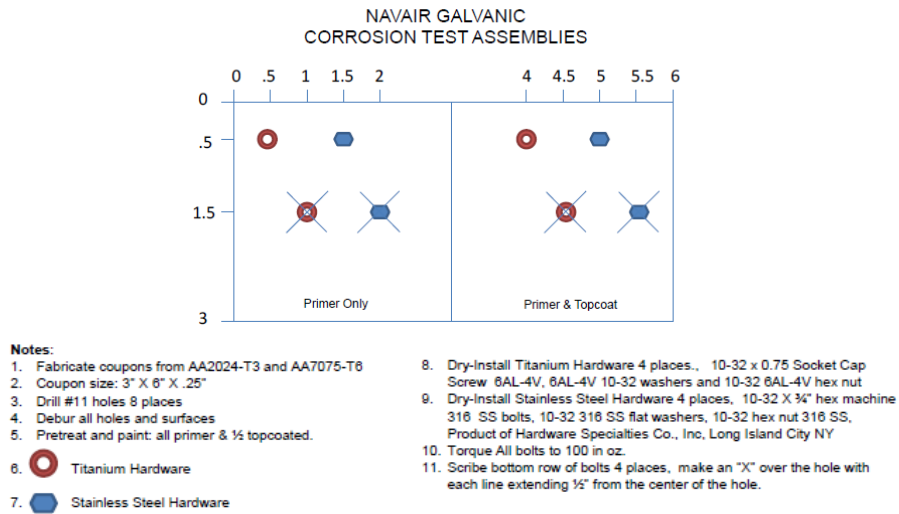
Present work combines experimental measurements of galvanic corrosion damage and computational modeling of galvanic current distributions. The effects of sample geometry, including spacing between fasteners and their location relative to the edges of the sample, as well as water layer thickness are investigated.

3.3 Method and Materials

Galvanic Corrosion Assembly

The development of a galvanically coupled fastener and painted Al alloy substrate assembly for the purposes of an accelerated test to provide rapid and accurate assessment of protective coating systems with a realistic structure in mind was the motivation behind the Naval Air Systems Command (NAVAIR) galvanic corrosion assembly being modeled in this work⁶.

This assembly shown in Figure 3.1a, contains the accurate measurements of the dimensions of the fasteners, washers, and panel which can be found in Tables 3.1 & 3.2⁷. The schematic of the fastener, washer, and panel configuration can be found in Figure 3.1b. In addition to these macroscale measurements, microscale measurements were needed to characterize the sizes of the gaps between the different components. These values were determined via cross-sectional metallography⁷. These results are shown in Figure 3.1c with the values used in the calculations discussed here highlighted in red.



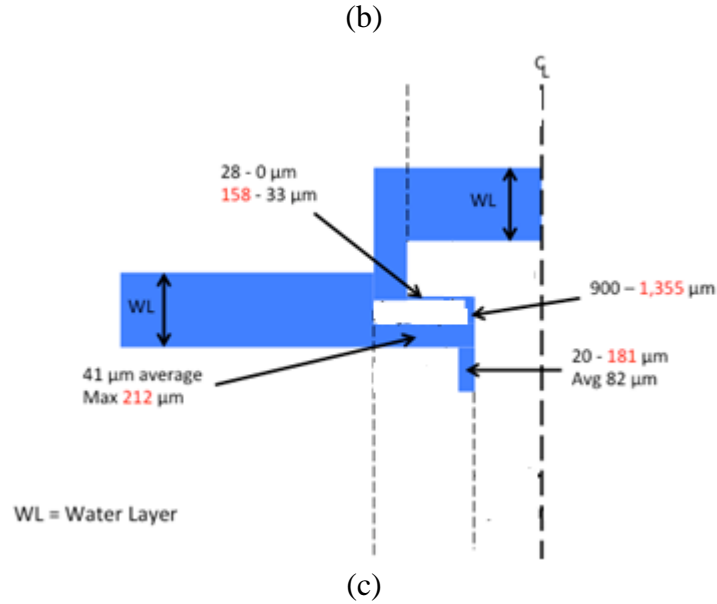


Figure 3.1: (a) NAVAIR galvanic corrosion assembly schematic⁶. (b) Schematic of the bolt to panel with the measurements found in Table 1&2. (c) Schematic of the spacing between fastener, washer, and panel with measurement used highlighted in red.

Table 3.1: Measurements of the outer and inner diameters of the washers

Washers	OD	ID	Thickness
316 SS	.7497 ± .0003"	.2088 ± .0003"	.0285 ± .0000"
Ti-6Al-4V	.4995 ± .0005"	.2190 ± .0000"	.0335 ± .0000"

Table 3.2: Measurements of the different fastener parts

Bolts 10-32 thread	<u>A</u> : Bolt head diameter	<u>B</u> : Height of cap	<u>C</u> : Length of threaded bolt	<u>D</u> : Diameter of bolt (outer thread-to- thread)
316 SS	.3023 ± .0003"	.1848 ± .0003"	.7357 ± .0000"	.1827 ± .0003"
Ti-6Al-4V	.3052 ± .0003"	.1863 ± .0003"	.7332 ± .0005"	.1827 ± .0003"

Three-dimensional finite element analysis (FEA) computational modeling

COMSOL Multiphysics FEA, solver and simulation software (v5.3) was used to develop a 3-dimensional model of the NAVAIR corrosion assembly of an AA7075 panel with SS316 and Ti-6-4 fasteners. This model geometry is shown schematically in Figure 3.2. The model was

based on the specifications outlined elsewhere⁶ to simulate the galvanic coupling between the fasteners and the panel.

This model was constructed within the corrosion module of COMSOL utilizing the secondary current distribution framework in stationary mode, which denotes no time dependence. To solve for the current distribution the Laplace governing equation $\nabla^2\Phi = 0$, where ∇^2 is the laplacian operator and Φ is the potential in the domain. The electrolyte potential (Φ_l) and the electric potential (Φ_s) were defined as dependent variables, along with the electrode and electrolyte regions being defined as domains. Within these domains, the current distribution was described by variations of Ohm's Law. For the electrolyte potential $i_l = -\sigma_l\nabla\Phi_l$ and the solid electrode $i_s = -\sigma_s\nabla\Phi_s$, where i_l and i_s are the current densities [A/m^2] in the electrolyte and electrode respectively. Similarly, σ_l and σ_s are the conductivities [S/m] and $\nabla\Phi_l$ and $\nabla\Phi_s$ are the potential gradients [V/m] in the electrolyte and electrode. To make this model simpler, the solid electrodes (AA7075-T6, SS316, Ti-6-4) were assumed to be perfect conductors with ohmic resistances equal to zero. This makes all spatial points on each of the electrodes to be equipotential making $\nabla\Phi_s = 0$. This assumption is valid due to the orders of magnitude difference between the resistivity's of the electrodes and the electrolyte solution. With this assumption made, the only remaining domain is the electrolyte domain where charge conservation was assumed and the divergence of the electrolyte current density is zero $\nabla \cdot \Phi_l = 0$. The edge of the model's domain were all denoted as insulated $-\mathbf{n} \cdot i_l = 0$ where \mathbf{n} is the normal vector of the boundary pointing into the electrolyte domain. The interface of the electrolyte and electrode were modeled by secondary current distributions, meaning the current density was a function of the over potential (η). Within this model, the over potential, which is the deviation of the corrosion potential according to $\eta = -\Phi_l - \Delta\Phi_{s, film} - E_{corr}$ where

$\Delta\Phi_{s, film}$ is the potential drop over a surface film and the E_{corr} is the corrosion potential of the metal/electrolyte system [V]. The conductivity of the electrolyte that was used for all simulations was 6 S/m. The solver utilized in this model was the MUMPS solver with a preordering allocation factor of 1.2 and a relative tolerance setting of 0.001.

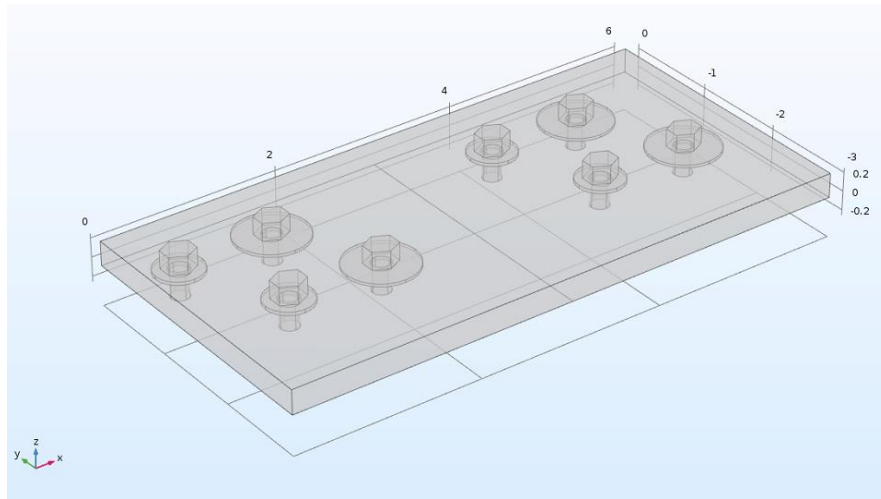


Figure 3.2: COMSOL model geometry of the NAVAIR galvanic corrosion assembly.

Construction of model in COMSOL

To construct the assembly within COMSOL utilizing the measurements provided by Luna Innovations, the geometry tab was used. Within this tab there are different operators that let one build, connect, or subtract the objects that are constructed. Each fastener was constructed separately utilizing the work plane operator to construct the head of the fastener to be extruded to the height specified in Table 3.2, the cylinder build operator to construct the washer and the bolt. The panel was constructed using the block build operator. After each of the coordinates for the fasteners were specified, the construction of the water layer was next. The construction of the water layer consisted of adding additional cylinders and blocks around each of the fasteners. The

finished construction can be seen in Figure 3.3 in which the 500 micron water layer can be seen overlaid on the fastener/panel.

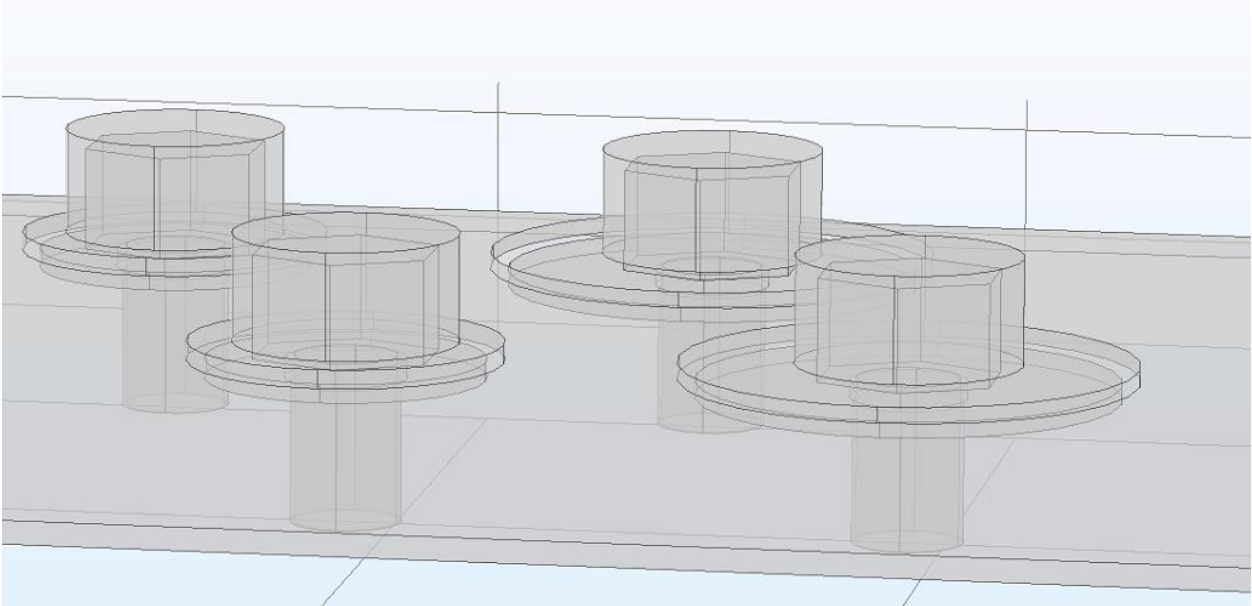


Figure 3.3: Final construction of the NAVAIR galvanic corrosion assembly.

Materials

Luna provided electrochemical boundary conditions determined from experimental measurements of polarization curves at 35 C. Data were generated for two kinds of fasteners (316SS, Ti-6-4) with and without a sol-gel coating. For the purposes of this work, the details of the formulation and application of the sol-gel coating are unimportant. The sol-gel acts to hinder the cathodic kinetics and it is that behavior that this work seeks to model. The open circuit potential (OCP) was measured for 1 hr before the polarization curve was generated. For the cathodic fastener materials, the scan was conducted from +100 mV vs. the OCP to -1 V(SCE) at a scan rate of 0.5 mV/sec. Both bare and sol-gel coated materials were measured. For the 7075-T6, the scan in Figure 3.4 was conducted anodically from -50 mV vs. the OCP to -0.2 V(SCE). The data for 7075-T6 in Figure 3.4 collected after the AA7075-T6 was polarized to -0.3 V(SCE))

for 1000 sec then scanned at 0.5 mV/sec until -1.2 V in order to simulate the surface that would be present in an activated localized corrosion site. For all materials, the polarization curves were measured in 5% NaCl. These boundary conditions can be seen in Figure 3.4.

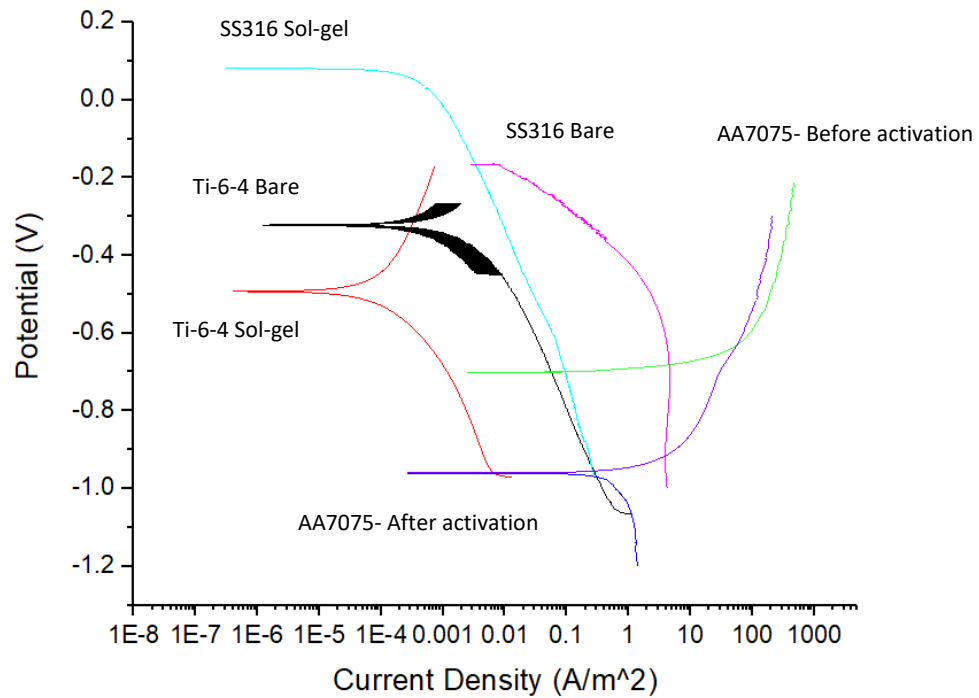


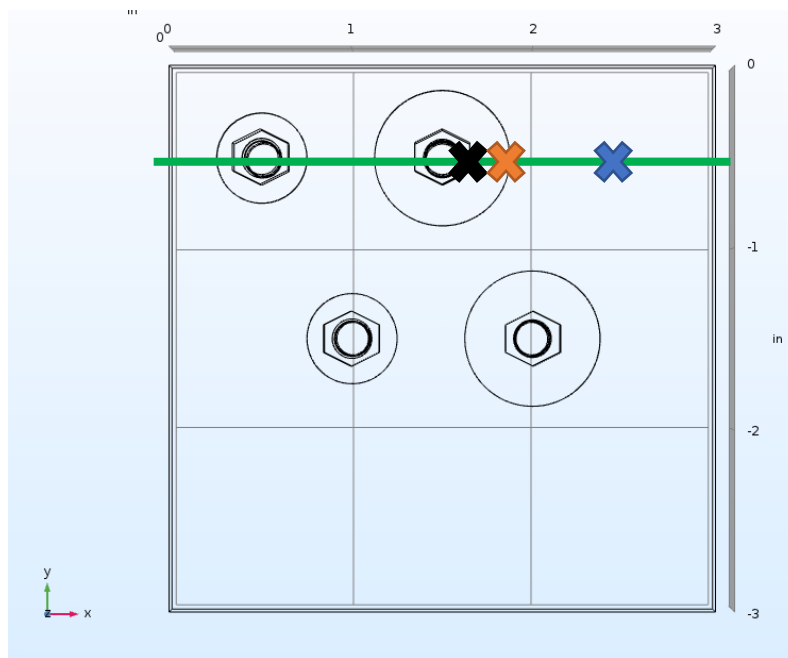
Figure 3.4: Polarization curves provided by Luna Innovations at 35C and 5% NaCl before activation of the AA7075-T651 and after activation of the AA7075-T651.

3.4 Results

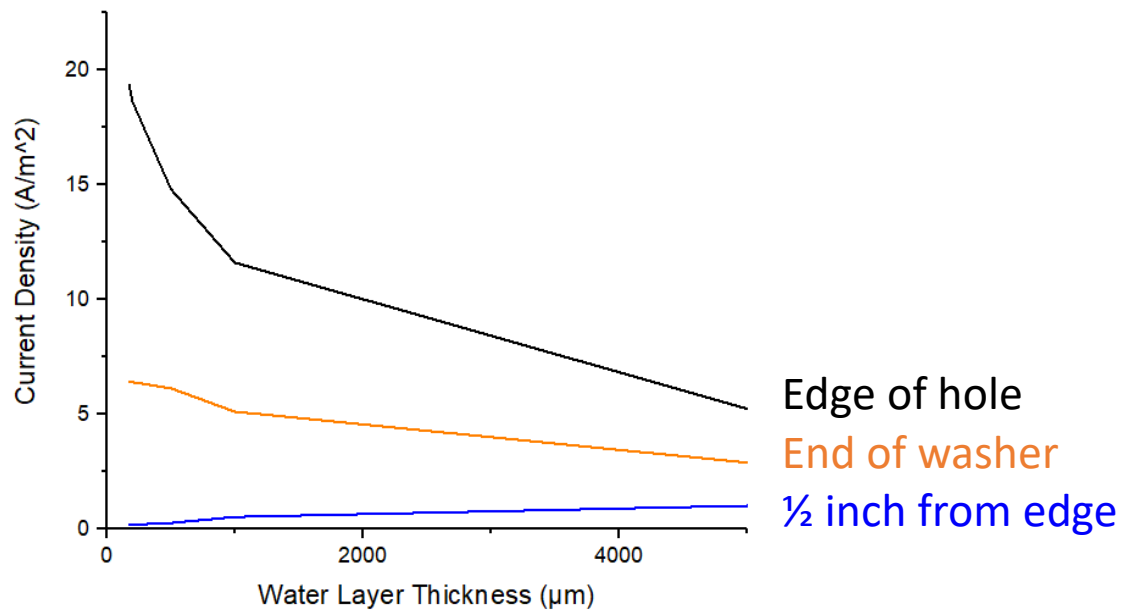
This galvanic corrosion assembly that was modeled yielded results consisting of the current density and potential distributions within the system. The graphs that are shown below are from ORIGIN using the data obtained from COMSOL. The false color plots are images obtained from COMSOL. The boundary conditions used in the following sets of data are from Figure 3.3a unless otherwise stated.

Water Layer Effects

Figure 3.5b shows the anodic current density on the AA7075-T6 as a function of water layer thickness at three unique locations shown in Figure 3.5a. These represent the edge of the hole (black X), the edge of the washer (orange X) and a position 0.5 in from the edge of the washer. The water layer thicknesses that were used varied from 250um to 5000um. The current density at the edge of the hole is the most intense at all water layers and both the edge of the hole and end of the washer locations see a decrease in current density as the water layer thickness is increased. The location that is a half inch from the edge sees a slight increase of current density as the water layer thickness is increased.



(a)



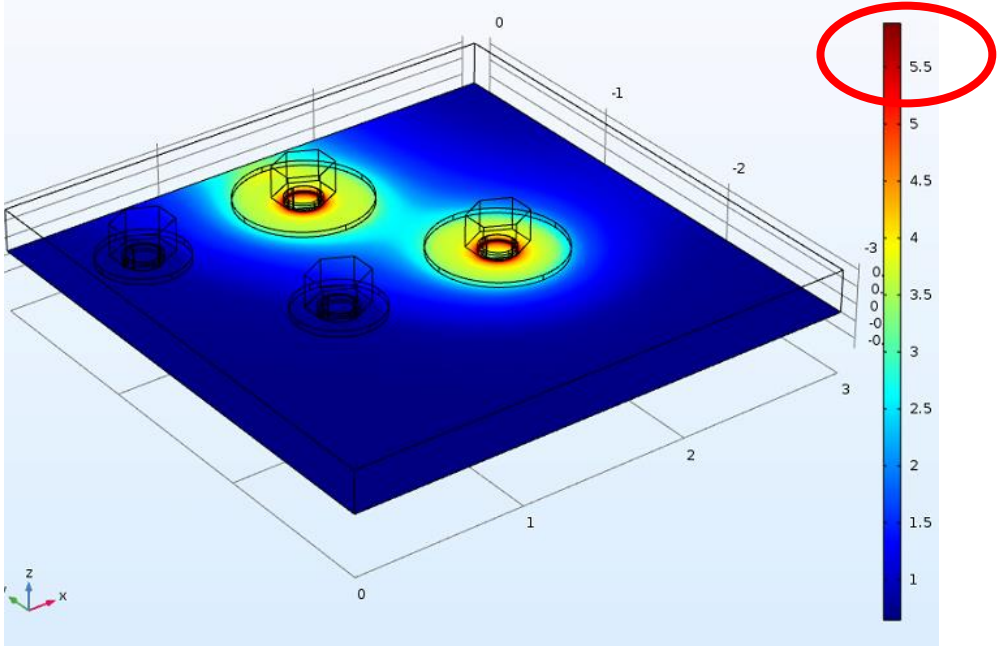
(b)

Figure 3.5: (a) Geometric layout of the three locations to be measured at varying water layer thicknesses. (b) Current Density distribution as a function of water layer thickness at three distinct locations found in (a).

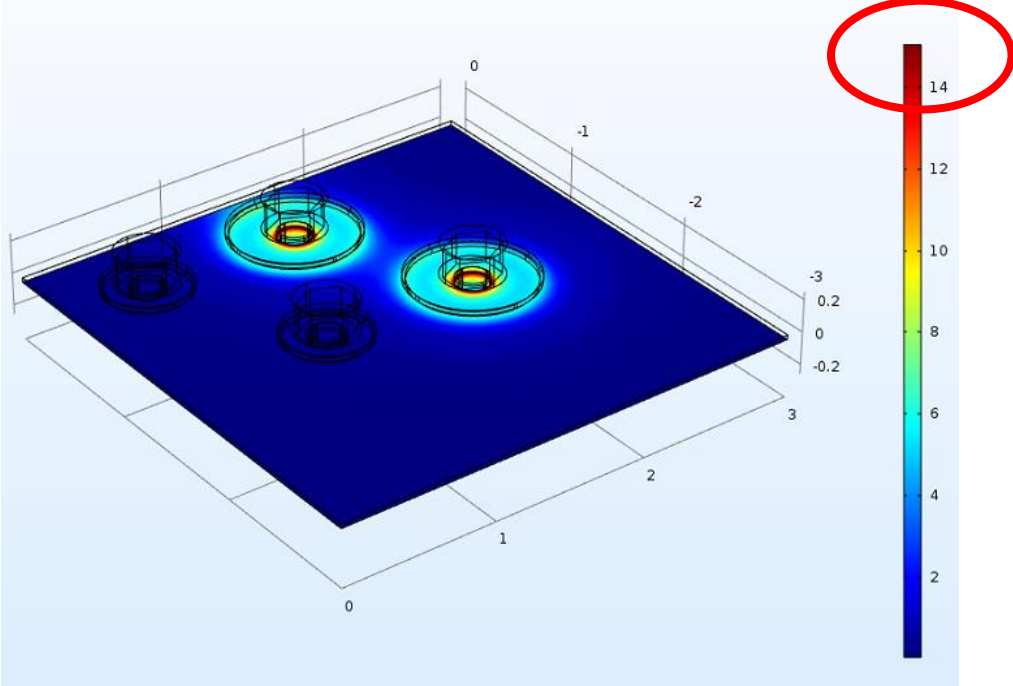
Conformal vs Uniform Water Layer

Figure 3.6 shows the difference in calculation when using either a uniform or a conformal water layer. A uniform water layer (Figure 3.6a) is one where the height of the water layer is measured off of the top of the fasteners, simulating a full immersion scenario, whereas the conformal water layer (Figure 3.6b) is one where the water layer is the desired thickness from all surfaces, simulating a thin film scenario. Highlighted in red are the differences in the maximum current densities and it is important to take note that even though the range of colors are similar, the scales are not. The uniform water layer leads to a broader distribution of the current, but the conformal water layer leads to much higher peak current densities at the edges of the holes. Within the uniform water layer, the stainless steel fasteners show that they interact with one

another, whereas in the conformal water layer, the stainless steel fasteners show much less interaction.



(a)



(b)

Figure 3.6: (a) Uniform water layer. (b) Conformal water layer. (Current densities are measured in A/m^2)

Edge Effects

Figure 3.7 shows a full NAVAIR galvanic assembly false color plot of the current densities (A/m^2). The only difference between the two sides are the fasteners location to the edge. The presence of the sample edges near the fasteners on the right and the one fastener on the left distorts the current distributions.

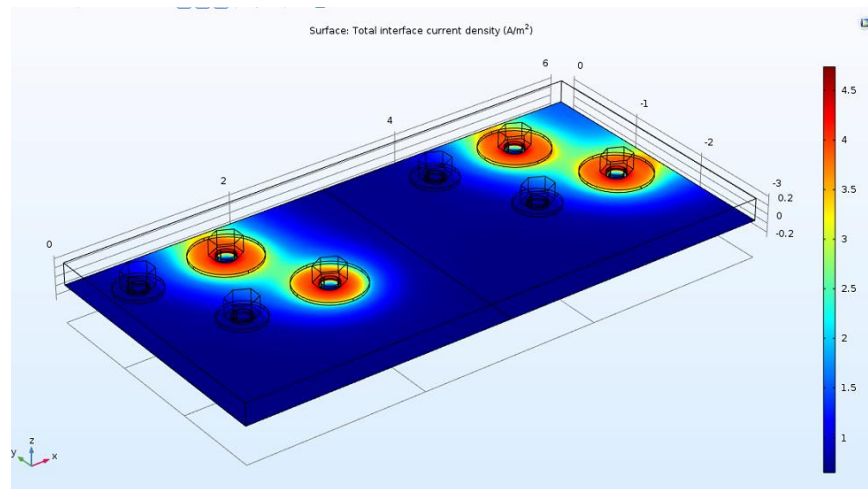


Figure 3.7: Current density false color plot of the full NAVAIR galvanic corrosion assembly showing the effect the edge has on the distribution.

Scribe Effect on Hole

The following figures in this section consider all areas of the AA7075-T6 panel to be perfectly insulated, except for the scribes as shown in Figure 3.8. The water layer thickness used was 1000 μ m, depth of the scribe was 100 μ m, width of the scribe was 150 μ m, and the length of the scribe was 0.4 in. In this figure the blue regions indicate where the AA7075-T6 boundary conditions were applied. This type of boundary condition closely mimics that of a wet-installed fastener, meaning the fastener is pre-coated before installment.

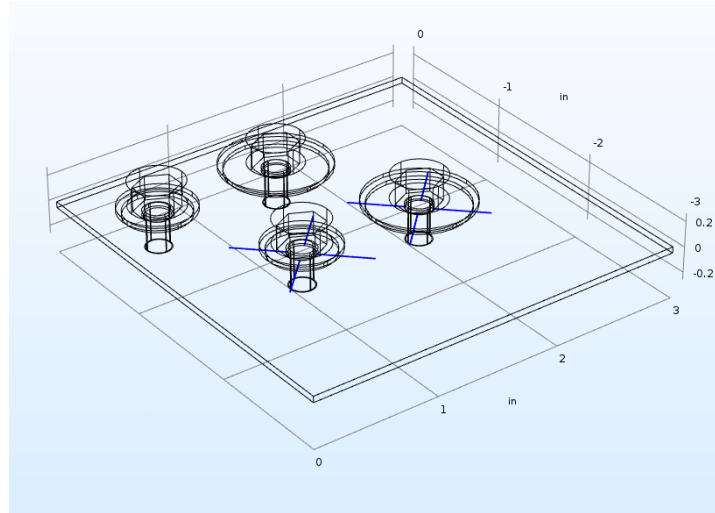
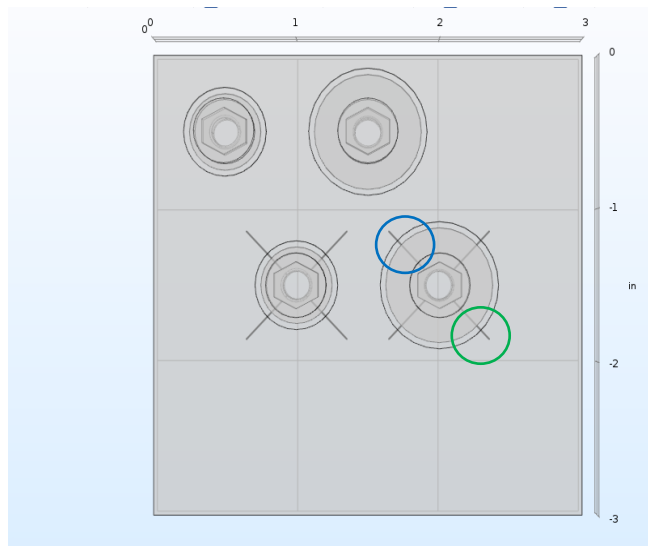
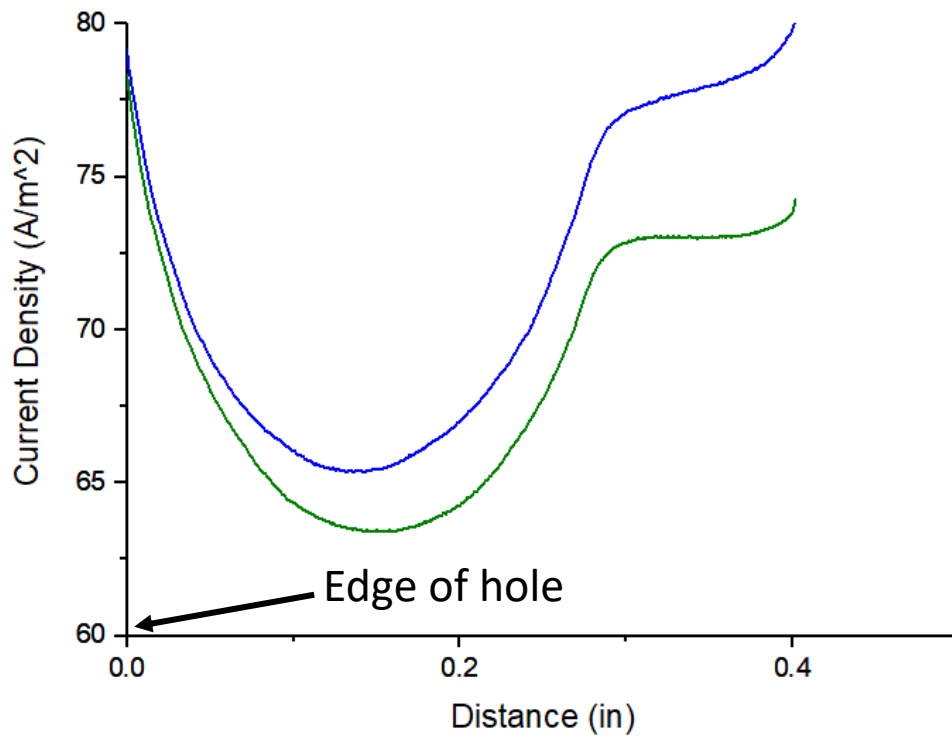


Figure 3.8: Illustration of the areas where the AA075-T6 boundary conditions were implemented in blue.

Figure 3.9 shows the effect that additional fasteners have on the current density along the scribe. Figure 3.9a shows the two scribes that are to be used for data collection. Figure 3.9b shows the current density of the scribes in Figure 3.9a and the distance is measured from the edge of the hole outward. The scribe that is closest to the additional fasteners (blue) experiences a larger increase of current density as it approaches the additional fasteners. The other scribe (green) does not experience as much influence from the additional fasteners, but has roughly the same current density at the edge of the hole.



(a)



(b)

Figure 3.9: (a) Illustration of the two scribe locations where the data is being obtained inside of the blue and green circle. (b) Current density distribution correlating to the colored circles in (a).

The following figures in this section consider all areas of the AA7075-T6 panel to be perfectly insulated, except for the scribes and holes, as shown in Figure 3.10. In this figure the blue regions indicate where the AA7075-T6 boundary conditions were applied. This type of boundary condition mimics that of a dry-installed fastener, which is when a fastener is installed with no coating. Even though this is not supposed to happen, it still occurs and the results of when it does are significant. The water layer thickness used was 1000um, depth of the scribe was 100 um, width of the scribe was 150 um, and the length of the scribe was 0.4 in.

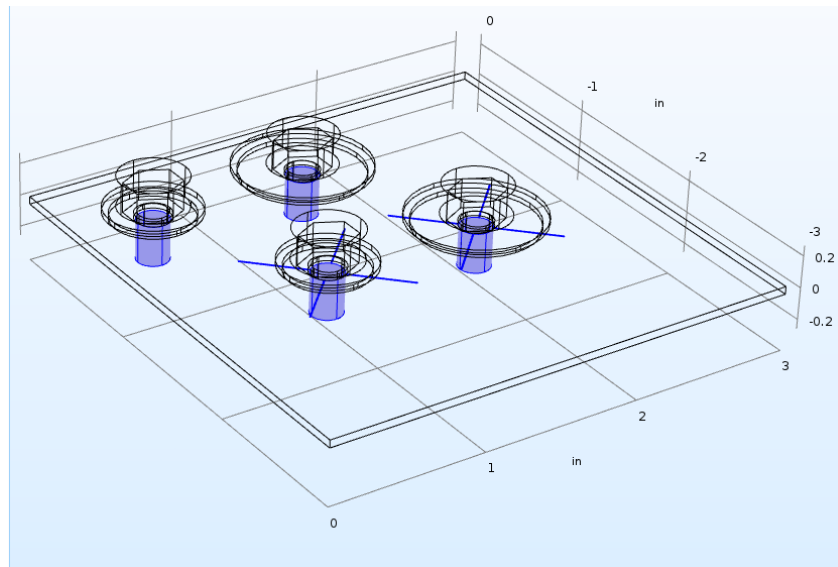


Figure 3.10: Illustration of the areas where the AA075-T6 boundary conditions were implemented in blue.

Using the boundary setup shown in Figure 3.10, the current density distribution following the path illustrated in Figure 3.11a was obtained for Figure 3.11b. The blue line corresponds to that of the hole, the orange to that of under the washer, and the green to that of the end of the scribe not under the washer. Outside of the washer the current density is at its highest and at the bottom of the hole, the lowest. There is a steady increase of current density while under the washer, however once outside of the washer, the current density levels off.

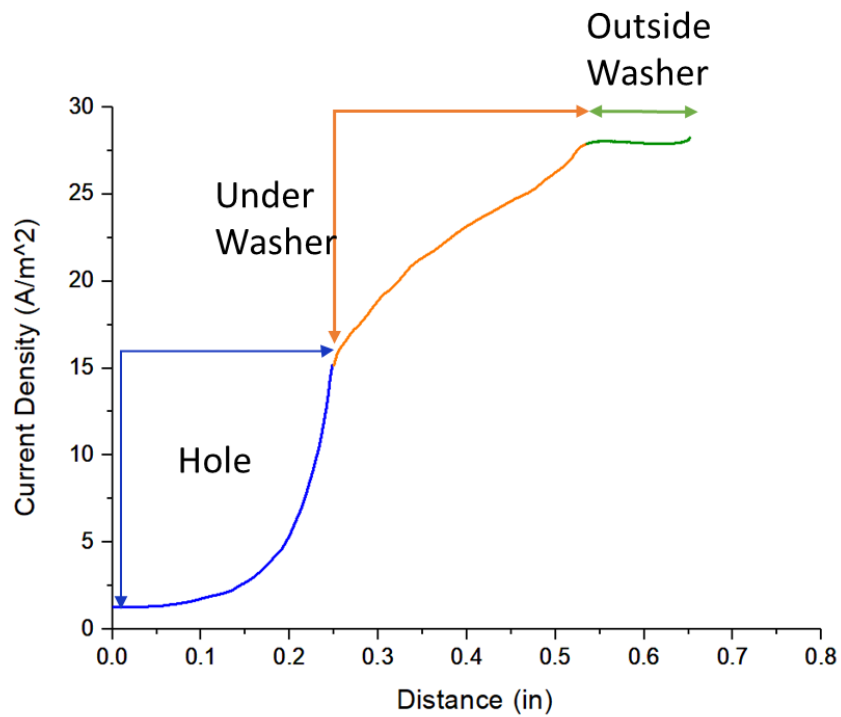
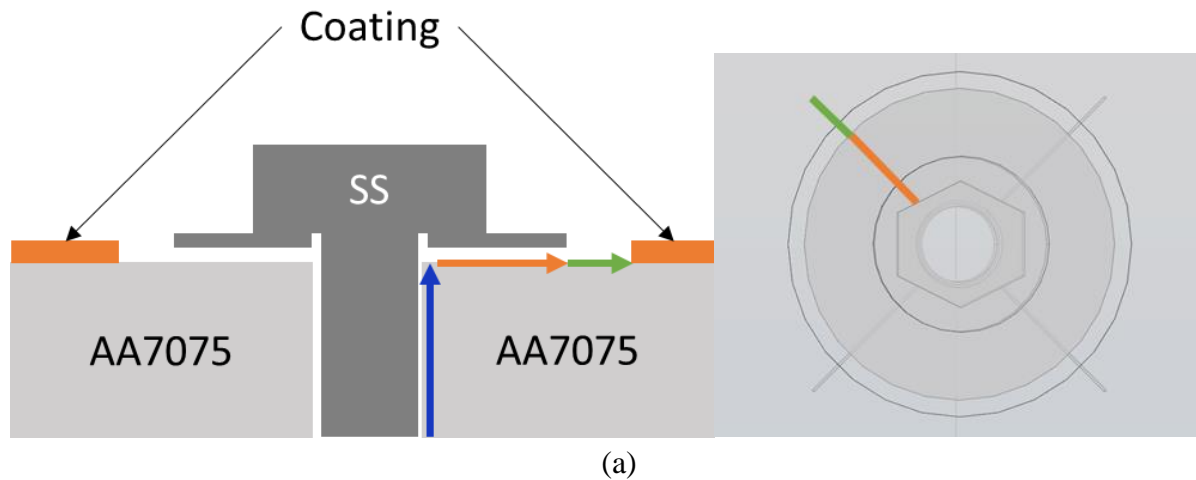


Figure 3.11: (a) Illustration of the path the data was obtained for (b) The current density distribution following the path illustrated in (a).

Using the data from Figure 3.9b and Figure 3.11b, excluding the hole, the two cases were compared to show the influence that the inclusion of the hole has on the current densities as shown in Figure 3.12. The bottom line (scribe with hole scenario) shows a large decrease of

current density compared to the top line (scribe only) with a decrease in current density as the edge of the hole is approached compared to the increase seen for the scribe only case. For both cases, the current density outside of the washer experiences little to no change.

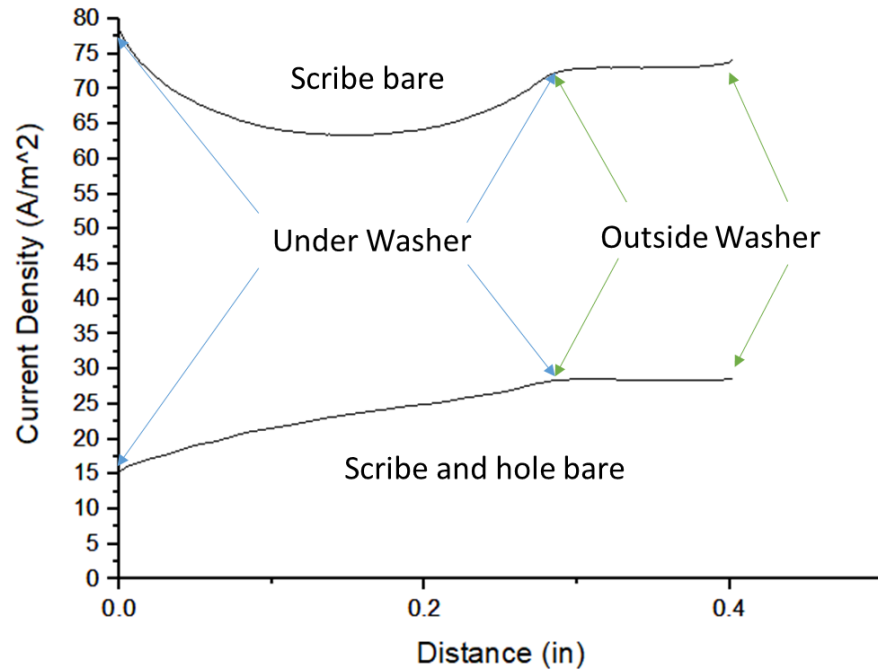


Figure 3.12: Current Density distribution comparing the two scenarios from Figures 8 & 10.

Effect of Sol-gel Application

In order to show the effects of sol-gel application onto the fasteners, the case of bare fasteners was evaluated as a base. The current density data were extracted along three lines shown in Figure 3.13a. The blue line intersects both stainless steel fasteners through the middle of where they show the most interaction, the green line intersects a Ti-6-4 fastener and a stainless steel fastener to show the difference in current density between the two, and the red line intersects both Ti-6-4 fasteners like the blue. Figure 3.13b shows the bare fastener scenario data and Figure 3.13c shows the sol-gel coated fastener scenario. For the bare case (Figure 3.13b),

the local maximums are seen at the edge of the hole and the end of the washer. Interaction between the two stainless steel fasteners can be seen as the current density does not approach zero between the two and only experiences no current density about a half inch away from the bottom stainless steel fastener. For the sol-gel case (Figure 3.13c), only around the stainless steel fasteners is any current density experienced, with a maximum at the edge of the hole and a steady decrease as the distance from the hole is increased. This current density experienced however, is almost one hundred times less than that of the bare case.

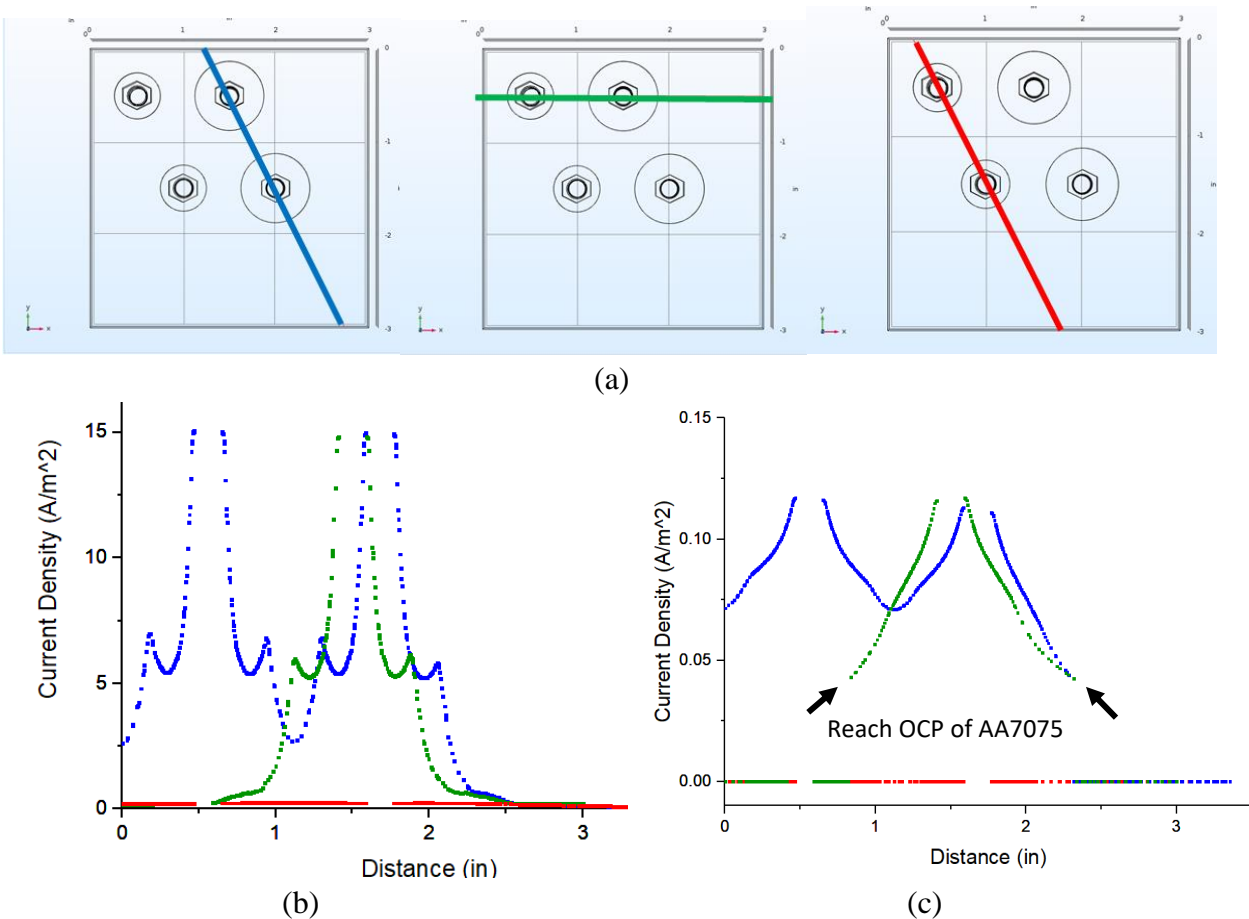


Figure 3.13: (a) Images with colored lines correlating to the data in (b) and (c). (b) Current density distribution of the bare case with the color of the line corresponding to the lines in (a). (c) Current density distribution of the sol-gel case.

Effects of Boundary Condition Variability

Using different boundary conditions on the same system can vastly change the results obtained. In order to show this, the boundary conditions shown in Figure 3.4 were used. To show how the data can change, the data obtained using these boundary conditions were put on the same graph as Figure 3.13b. In Figure 3.14a the current densities from the boundary conditions of Figure 3.4 the isolated curves from 3.14a of the after activation AA7075 being used is about half those of the before activation. Looking at Figure 3.14b, the same trend can be seen as found in 3.13a, however at a lesser scale. The Ti-6-4 fastener in the after activation case has a larger effect on the system compared to its counterpart.

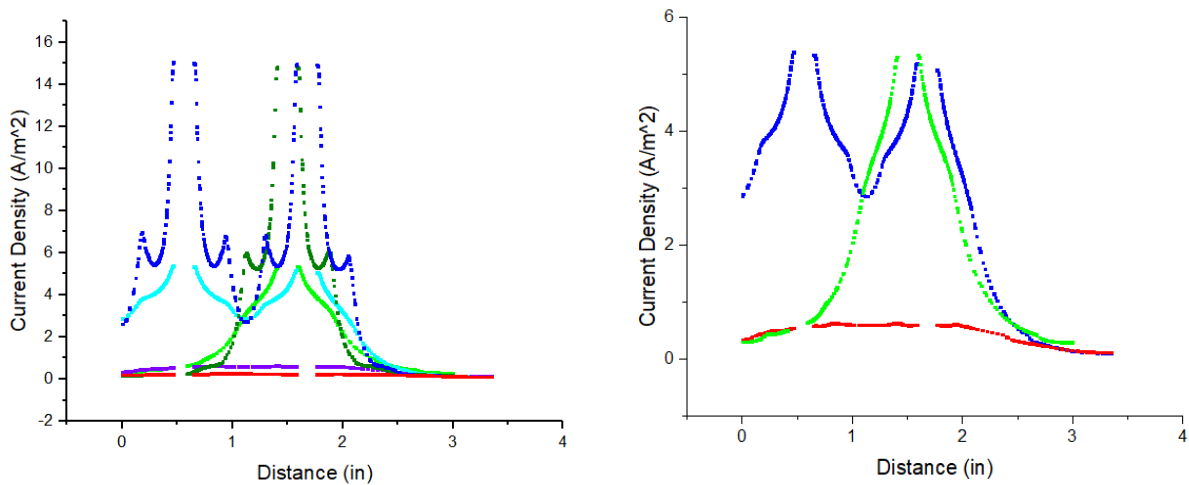


Figure 3.14: (a) Current density distribution with both boundary condition scenarios. (b) Current density distribution using the AA7075 boundary condition after activation.

3.5 Discussion

In this work there were two main effects that were explored: those related to geometric effects, and those related to boundary condition effects. The geometric effects that should be highlighted are the water layer thickness, presence of a nearby sample edge, and how the hole

interacts with the scribe. The boundary conditions also play a role in how current distributions within a model are solved. The boundary condition effects that should be highlighted are the effects of sol-gel application and the variability in boundary conditions.

Geometric Effects

The geometric effects that were highlighted in the results section (water layer, edge, and hole) all interact with one another and show similar trends. One of these trends is that at the edge of the hole is where the highest current density is experienced, this can be seen in in Figures 3.5, 3.6, 3.7, 3.9, 3.13, and 3.14. The next local maximum for these figures was at the edge of the washer. These two locations having the two local maximums could be explained by the area ratio between cathode and anode surrounding these two points with under the washer being able to “pull” current from the fastener it is closest to and the end of the washer being influenced by not only its own fastener but the most adjacent fastener. This interaction between fasteners is visible in Figures 3.6, 3.7, 3.9, 3.13, and 3.14 where the current density does not approach zero before approaching another fastener. The effect of this interaction however is controlled to some extent by the water layer thickness, as thinner water layers will inhibit the ability of the fasteners to “throw” their current to adjacent fasteners and thus focus the current at closer locations, as seen from Figure 3.5, which shows the decrease in current density at the edge of the hole and end of the washer as the water layer thickness is increased. All of these figures were under the same condition of having the entire plate be the domain where the AA7075-T6 boundary condition was applied. For the case of a scribed, coated sample with and without the hole included, the effects of the fastener interaction and the suppression of current density due to a hole were seen. This latter effect is important to note due to the idea that some holes could be coated and as

shown, this would lead to a very intense attack along the edge of the hole should the coating fail on the surface.

Boundary Condition Effects

The boundary condition effects that were highlighted in the results section (sol-gel application and variability in boundary conditions) show the importance of utilizing the correct boundary conditions when trying to mimic an experiment. As shown in Figures 3.13 and 3.14, which uses a different boundary conditions for the plate, using different boundary conditions can give you a very different solution. It is important to note that the only difference between the boundary conditions in 3.13b and 3.14b is the AA7075-T6 boundary conditions used in 3.14b are taken after activation of the surface. This activation is meant to represent the anodic kinetics of a localized corrosion site that is actively growing. The AA7075-T6 kinetics used in Figure 3.14a confound both initiation of localized corrosion and its propagation. Knowing how the use of real experimental data as the boundary conditions within a model affect the solution of the model, it is important to remember that in order to be able to correlate data between the two, the data used needs to be correct.

3.6 Conclusion

The COMSOL model was run under a variety of boundary conditions and geometric set ups to obtain different solutions. The influence of geometric and input boundary conditions were investigated, as well as the ability sol-gel coating.

- (1) The water layer thickness plays a large role in the ability of fastener interaction and the intensity of attack at the edge of the hole. With larger water layer thicknesses causing more fastener interaction and less intensity at the edge of the hole.

- (2) The edge of the hole sees the most intense current density on a bare plate and when the plate is considered perfectly insulated (coated scenario), the edge of the hole's current density is suppressed with the presence of an uncoated hole.
- (3) The ability for the model to come to a solution that can be used for comparison to experimental data depends on the input of correct boundary conditions as the variability from boundary conditions is high.

3.7 References

1. Corrosion of Aluminum and Aluminum Alloys, J. R. Davis, Editor ASM, Materials Park, OH (1999)
2. J.X. Jia, A. Atrens, G. Song, T.H. Muster, Simulation of galvanic corrosion of magnesium coupled to a steel fastener in NaCl solution, *Materials and Corrosion* 56 (2005) 7, p. 468-474
3. D. Hawke, T. Ruden, Society of Automotive Engineers, [Special Publication] SP, 1995, SP-1096, 63–67.
4. J. I. Skar, *Materials and Corrosion* 1999, 50, 2.
5. G. Gao et al. in: The 2nd Israeli International Conference on Magnesium Science & Technology 2000, Dead Sea, Israel.
6. C.A. Matzdorf, W.C. Nickerson, B.C.R. Troconis, G.S. Frankel, L. Li, R.G. Buchheit, *Corrosion* 69 (2013): p. 1240-1246
7. Liu, C., Kelly, R.G. Final Report to Luna Innovations (2015).

4 Summary, Technological Impact, & Recommendations for Future Work

4.1 Summary

Chapter 2: Automated Quantification of Corrosion Damage from Cross-sectional Micrographs

A digital image analysis algorithm was developed to perform several tasks researchers could find useful. The work shows capabilities and limitations of the algorithm through examples including depth profile measurements, histogram outputs, and tilt correction. The algorithm was tested against other methods and showed a large decrease in time to process an image from between 1 hour to 3 hours for a manual method to 10 second to 60 seconds using the algorithm.

Chapter 3: Computational studies of potential and current distributions on complex geometrical structures involving galvanic couples under thin electrolyte layer conditions

A geometrically complex model was constructed in COMSOL™ to investigate geometric effects and the application of real-life experimental data as boundary conditions. Through many different simulations, the work shows that water layer thickness affects the ability for fasteners to interact, the degree of intensity of attack at the edge of the hole, and the ability to incorporate real-life experimental data as boundary conditions to obtain data to be used in correlation with experiments.

4.2 Technological Impact

- *Development of a Damage Quantification Tool*

There was a need for a tool that would allow researchers the ability to quickly and accurately evaluate different types of localized corrosion on cross-sectional micrographs.

By developing this open-sourced algorithm, researchers will be able to obtain more data

than previously possible allowing for the opportunity to make more conclusions that were not possible before due to lack of data.

- *Application of Real-life Experiment Data used in Simulations*

With the use of real polarization curves in this work, the opportunity to model situations encountered in experiments and industry is possible. The results of this work resemble that of the findings by Z. Feng and G.S. Frankel in “Galvanic Test Panels for Accelerated Corrosion Testing of Coated Al Alloys: Part 2—Measurement of Galvanic Interaction” where they found that the galvanic interaction between fasteners was observed such that the cathodic current of other fasteners was decreased when a new fastener was added. Scribes on a panel can interact with distant fasteners, not just the closest ones. The amount of corrosion as determined by charge and optical profilometry were close and indicated SS316 fasteners caused more corrosion attack than Ti-6Al-4V fasteners, which also is explained by differences in the cathodic current of the fasteners¹.

- *Complex Geometrical Models can be easily Implemented*

With the construction of a complex geometrical model in this work, it demonstrates the ability to construct a model that uses secondary current distribution with a complex structure. Currently there is little work done with constructing models in 3D as many models can be reduced to 2D due to symmetry, this work shows that if the experiment to be modeled is at all complex, using a 2D model will not show the full effects that occur due to geometry, such as the edge effects as seen in Figure 3.7.

4.3 Recommendations for Future Work

The current work filled the need for a tool for damage quantification and the ability to incorporate real experimental data within a complex model. This work can be used as a framework to further the understanding of more advanced research in the following areas:

- *Expanding the ability of the algorithm to refine its resolution*

Currently, the algorithm has some limitations with discerning extremely fine fissures without the help of an additional image at higher resolution. Work into refining the resolution of detecting a border would allow the algorithm to detect more fissures and increase the accuracy of measurements.

- *Increasing the capability of the algorithm to be more automatic*

The algorithm as it is now has the ability to go through images and upload the data into either a cvs or excel file for each image typed into the algorithm. Adding a loop function to pre-select images within a folder would allow for quicker data acquisition.

- *Finding quantitative correlation between model and experimental work*

The model and simulations presented here have found qualitative correlation with experimental work, however quantitative correlation is needed. With quantitative correlation comes the ability to not only predict where damage will occur, but the severity as well. This will also allow for the validation of results in the model going forward.

- *Testing image analysis algorithm against a known sample*

To test the validity of the algorithm, look into comparing the accuracy of the algorithm through lithography. By doing this, the algorithm can be validated or fine-tuned in order to give the best results.

4.4 References

1. Z. Feng, G.S. Frankel, *Corrosion* 70 (2014): p. 95-106

5 Appendix

5.1 Algorithm

Border.m

```
location='BareB7';%file path minus type extension goes here
pic=strcat(location,'.png');%change this extension if the file is not a jpg
img = imread(pic);%this reads a file ( you must type in the file name and be sure that it is in the
same folder as this script)
I = rgb2gray(img); %changes image from rgb color scheme to gray
[x,map] = gray2ind(I,100); %take the image and maps the gray scale to 100 different shades
bw2=im2bw(x,map,0.45); % takes the gray scale and makes it black and white
wb = imcomplement(bw2); %changes the image to white and black (inverse the black and white)
regionwb=bwareaopen(wb,300); %this takes any area that is 350 pixels or less and fills it with
black you can see this from figure 1 to 2
region_borders1 = imdilate(regionwb,ones(3,3)) > imerode(regionwb,ones(2,3)); %this will
make the border of the image
region_borders2 = bwareaopen(region_borders1,300);%Found this way to be a better way of
producing the border Included previous version to show you the difference
rb3=imcomplement(region_borders2);
figure1=figure;
imshow(rb3,'InitialMagnification','fit')
```

DepthAnalysis.m

```
boundaries = bwboundaries(rb3,'noholes');
X=boundaries(3,1); %Change first number in order to obtain border in question
Y=X{1,1};
I = find(Y(:,2)==max(Y(:,2)));
Yx=min(I); %finds where the border turns to an edge
plot(Y(1:Yx,2),Y(1:Yx,1))
maxy = min((Y(1:Yx,1)));
%maxy=57.59; %This is where you type in the value you found from measuring in Image
viewer
Z = (Y(1:Yx,1))-maxy;
hold on
line('Xdata', [0 Yx],'Ydata', [maxy maxy])
hold off
Micro_per_pixel = 500/80;%second number is for scale bar pixels
DifferenceY = Z*Micro_per_pixel;
figure2=figure;
Xunit= (Y(1:Yx,2))*Micro_per_pixel;
DifferenceX=min(Xunit);
Xunits=(Y(1:Yx,2))*Micro_per_pixel-DifferenceX;
plot(Xunits,DifferenceY)
MaxCoated=max(Xunits);
% lowerbound=2000; %sets lower and upper bounds of the x scale to linearize
% upperbound=6000;
```

```

% unos=zeros(length(Xunits(lowerbound:upperbound)),1);
% unos(:,1)=1;
% X=[unos Xunits(lowerbound:upperbound)];
% B=X\DifferenceY(lowerbound:upperbound); %generates solution matrix that carries the
slope of the edge of the sample
% theta=-atan(B(2)); %theta is the angle of rotation...may be hard coded...USE THIS
COMMENTED OUT SECTION IF IMAGE NEEDS ROTATING
% rotate=[cos(theta) -sin(theta);sin(theta) cos(theta)];
% flat=[Xunits DifferenceY]*rotate; %rotates DifferenceY matrix...should be flat
% maxy2=min(flat(:,2));
% figure
% plot(flat(:,1),flat(:,2)-maxy2)
% corrLength=flat(:,2)-maxy2;
name=strcat(location,'_histogram');
figure3=figure;
histogram(DifferenceY) %use 'DifferenceY' matrix if pic does not need rotating, use
'CorrLength' matrix' if it does
title('INPUT TITLE HERE') %Title for Histogram chart
xlabel('Damage Depth ({\mu}m)')
ylabel('Frequency')
saveas(figure3,'name_histogram.jpg')
MaxCorr=max(DifferenceY)%max corrosion damage...use 'DifferenceY' matrix if pic does not
need rotating, use 'CorrLength' matrix' if it does
MeanCorr=mean(DifferenceY)%mean corrosion damage...use 'DifferenceY' matrix if pic does
not need rotating, use 'CorrLength' matrix' if it does
filename='Input Name.xlsx'; %change name here for excel sheet
xlswrite(filename,Xunits,'Sheet2','A1');
xlswrite(filename,DifferenceY,'Sheet2','B1');
M=[Xunits,DifferenceY];
csvwrite('Input Name',M,0,2);

```

5.2 User Manual

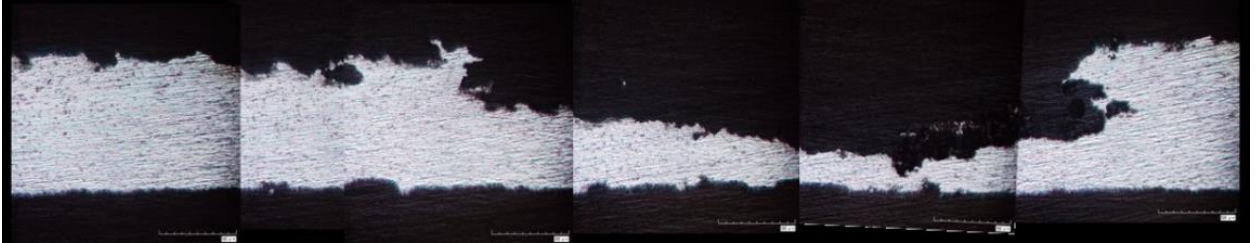
Objective

The goal of this code is to take a horizontal-rectangular cross sectional photo and obtain more data than other methods, primarily ImageJ. Using this code you will be able to obtain a depth profile, total un-corroded area, histogram of the depth profile, mean depth, and max depth. There is also an option to export raw data into Microsoft excel. It is important to note that you will need a **scale bar on the original photo** so you can obtain values that are not in pixels.

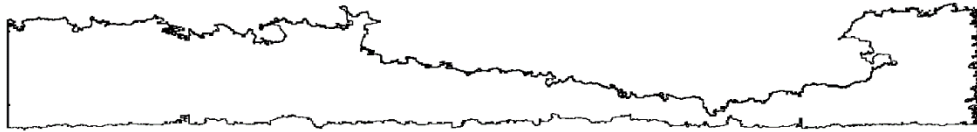
How to Use

1. Have MATLAB installed on computer. If you do not have MATLAB installed, UVA has a remote desktop you can use called the HIVE. Here is the link to get this installed <http://its.virginia.edu/hive/connected.html> .

2. Ensure that there is **black** on the **sides** of the photo as pictured below. This will make certain that there is a complete border. If your photo does not have black on the sides, an easy fix is to paste your photo in paint and slightly move it to the right and use the bucket with black paint and fill the background as black.



3. Open the Script **Border.m**
4. In order to use this code you must have the photo inside of the same folder as the scripts (the code). On line 1 of the code, change the name in between the ‘ ‘ to your photo’s filename.
 - a. If your photo is not a .jpg change the extension in line 2 of the code to your extension.
5. Run the script by going to the editor tab at the top and clicking Run. This step is to check to see if you need to make any changes to line 7’s threshold value. The picture that the script releases labeled Figure 1 should resemble the black and white photo on the top of the next page.



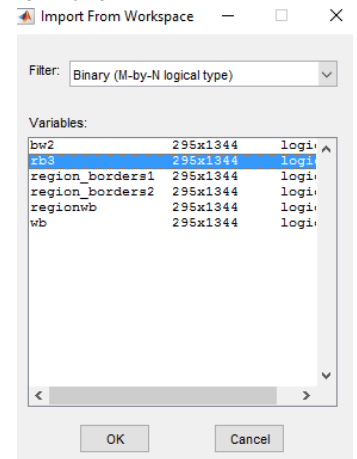
- a. If the photo does not resemble this, change the number value in line 7 between the values of 0 and 1 until you receive a photo that matches your original photo and is a complete border.
 - b.
6. Open the app in MATLAB called Image Region Analyzer
 - a. This is found in the Apps Tab under Image Processing and Computer Vision, if this is not at the very top of your apps selection, click the black arrow at the end of the toolbar.

7. After opening Image Region Analyzer, you want to load in rb3 from the workspace.

a. You can get to this option by clicking the down arrow on the load image button pictured to the right and select import from workspace.



b. You will then get a screen that will give you a lot of options and you want to select rb3 and press OK. Pictured to the right.



8. This will open your photo with a table on the right. You will want to select the value in the Area Column that fills in the border with **RED**.

a. Select the large numbers until you get the correct one which should look like the picture below.

b. This value is the Total Un-corroded Area, measured in pixels which you can convert to your unit of measurement with the scale bar in the original photo.

c. Take note of the row number, this will be the value that you plug into line 2 of the script **DepthAnalysis.m** to create the correct border.

	Area	MajorAxisLength	MinorAxisLength	Eccentricit
1	276548	1.4983e+03	391.6150	0.96
2	9	6.1109	2.2857	0.92
3	108968	1.6158e+03	150.0866	0.99
4	1	1.1547	1.1547	
5	2	2.3094	1.1547	0.86
6	4	4.6188	1.1547	0.96
7	4	2.3094	2.3094	
8	3	3.4641	1.1547	0.94
9	4	4.6188	1.1547	0.96
10	1	1.1547	1.1547	
11	1	1.1547	1.1547	
12	2	2.3094	1.1547	0.86
13	4	3.6515	1.8257	0.86
14	9	6.2620	2.5526	0.91
15	6	3.4641	2.3094	0.74
16	4	4.6188	1.1547	0.96
17	1	1.1547	1.1547	
18	1	1.1547	1.1547	
19	2	2.3094	1.1547	0.86
20	3	2.5820	1.7638	0.73
21	2	2.3094	1.1547	0.86
22	1	1.1547	1.1547	
23	1	1.1547	1.1547	
24	2	2.3094	1.1547	0.86
25	2	2.3094	1.1547	0.86
26	1	1.1547	1.1547	
27	6	3.4641	2.3094	0.74



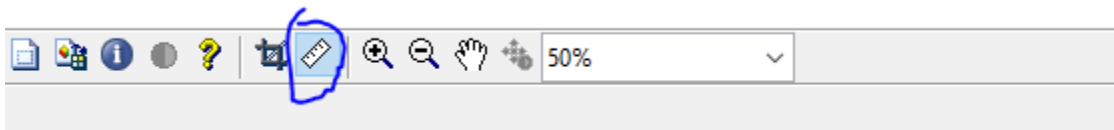
9. Open the script **DepthAnalysis.m** and on line 2 input the row number you figured out in step 8.

a. You will need to put this number in the x portion of the parenthesis (x,y)

10. Open the App Image Viewer, which is in the same tab as the Image Region Analyzer in Step 6-7.

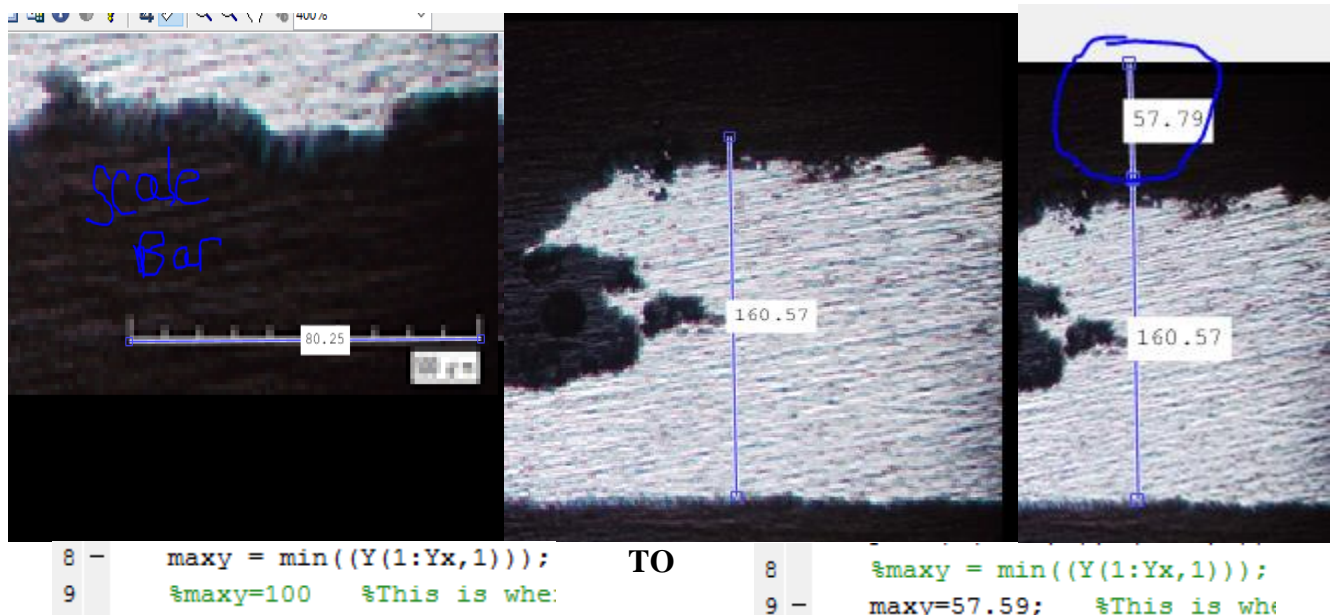
a. Once the app is open, use the file tab and open your original photo

b. First zoom in on your scale bar so that it takes up the whole screen and use the ruler tool pictured below to measure how many pixels the scale bar is



c. Take note of this value as you will need to use this later for line 14

- d. At this point, if you have a part of your sample that is un-corroded in the photo move on to step 11, if you do not continue to step e.
- e. This will take prior knowledge of how thick your sample was and converting that into pixels using the value you measured in step 10 b.
- f. Once you know this value, use the ruler tool and measure out this amount of pixels starting at the bottom of the sample.
- g. Now from that point measure to the top of the entire photo. **THIS** is the value you will type into line 8. Below is a series of photos showing this assuming the sample was 1000 μm and the scale bar was for 500 μm .
- h. Be sure to switch the % from line 8 to line 7 as depicted below.



11. In line 14, change the ration to fit your scale bar ratios.
 - a. The default currently is 500 μm to 80 pixels
 - b. Feel free to change `Micro_per_pixel` to a different name but be sure to that when you start to rename it to **SHIFT+ENTER** when done to switch all places where this function is used in the code switches also.
12. To change how the Histogram is labeled in line 37 you can change the title by changing the words from `INPUT TITLE HERE` to the title you wish.
 - a. The same goes for lines 38 and 39 with changing the y and x axis labels.
 - b. For greek letters, the correct way to type them is `{\GREEK LETTER NAME}`
 - c. In line 40 you can change the name of what the Histogram will be saved as in the folder.
13. This is **IF** you want to export the data into excel.

- a. On line 43, in purple there is written Input Name, this is where you type in the name of the file you wish to create. The program will create a new excel with this name in this folder.
 - b. The following two lines 44 and 45 are where it writes the raw data from the first graph (Depth Profile)
14. Line 47 writes a .csv that has columns separated by , and rows by ,,
- a. Type in the name you want where it says Input Name
 - b. This is an alternative to data storage from excel, if you wish to not have excel simply delete the lines that deal with excel
15. Click Run in the Editor Tab
- a. You should get 2 figures
 - i. Depth Profile
 - ii. Histogram
 - b. In the command window you will receive MaxCorr and MeanCorr which correlate to max depth of the corrosion and the Mean corrosion depth both in the units you specified with the conversion from **Step 11**.

Rotated Pictures

1. If the image taken is not level, you may wish to rotate it to receive more accurate data. The commented out code from lines 22-37 can be utilized to solve this. This portion of the code estimates a slope for the edge of the sample, finds the angle between that slope and the x-axis, and then rotates the plot of corrosion damage so that it is flush with the x-axis.
 - a. To generate the slope, a linear portion of the corrosion damage plot is selected by observation. The variables 'lowerbound' and 'upperbound', in lines 22 and 23, respectively, set endpoints in terms of indices of the 'DifferenceY' matrix. Make sure that these are in terms of indices (not microns or pixels) and that they represent a flat part of the edge.
 - b. Using matrix math, the angle between the edge and the x-axis is found in line 29. If the resulting figure that is displayed does not accurately rotate the image to flat, either the lower and upper bounds may be changed, **OR** you may simply multiply the value of 'theta' in line 29 by a scalar, which is often easier.
 - c. Additionally, if you have noticed that the plot was rotated clockwise instead of counterclockwise (or vice versa), you may change the sign of theta in line 29 by simply adding or removing a negative sign. This stems from the fact that the "rotation matrix" used in line 31 is used for rotating points counterclockwise, when indeed a clockwise rotation is sometimes necessary.

More on Exporting

1. For excel if you wish to continue using same file and have the data all on the same workbook you have two options, change the sheet it is exported onto for each photo or different columns on the same sheet.
 - a. To change the sheet number, simply change the number after 'Sheet1' to 'Sheet2'.
 - b. To keep the data on the same sheet but different columns change 'A1' (for x data) and 'B1' (for y data) to either 'C1' and 'D1' respectively or if you want a space in between 'D1' and 'E1'.